
Article:
Tao, X., Li, X., Dong, H. et al. (2 more authors) (2021) Evaluation of the sliding wear and corrosion performance of triode-plasma nitrided Fe-17Cr-20Mn-0.5N high-manganese and Fe-17Cr-35Ni-1.2Si high-nickel austenitic stainless steels. Surface and Coatings Technology, 409. 126890. ISSN 0257-8972

https://doi.org/10.1016/j.surfcoat.2021.126890

Evaluation of the sliding wear and corrosion performance of triode-plasma nitrided Fe-17Cr-20Mn-0.5N high-manganese and Fe-17Cr-35Ni-1.2Si high-nickel austenitic stainless steels

Authors:

Xiao Tao[a, b*], Xiaoying Li[b], Hanshan Dong[b], Allan Matthews[c], Adrian Leyland[a*]

Affiliations:

[a]Department of Material Science and Engineering, University of Sheffield, Sheffield, S1 3JD, United Kingdom

[b]School of Metallurgy and Materials, University of Birmingham, Birmingham B15 2TT, UK

[c]School of Materials, The University of Manchester, Manchester, M13 9PL, United Kingdom

Corresponding author*:

Dr. Adrian Leyland, Email: a.leyland@sheffield.ac.uk

Telephone: +44 (0) 114 222 5486

Fax: +44 (0) 114 222 5943

Full postal address: Department of Materials Science and Engineering, Sir Robert Hadfield Building, Mappin Street, Sheffield, S1 3JD, United Kingdom

Dr. Xiao Tao, Email: x.tao@bham.ac.uk

Full postal address: School of Metallurgy and Materials, University of Birmingham, Birmingham B15 2TT, UK

Keywords:

expanded austenite, plasma nitriding, sliding wear, aqueous corrosion, stainless steels

Abstract

Low-temperature plasma nitriding has been widely studied and applied, in enhancing the wear performance of austenitic stainless steels (ASSs) without losing corrosion resistance. In this work the wear and corrosion behaviours of two specialty ASSs, i.e. Staballoy® AG17 (Fe-17Cr-20Mn-0.5N, in wt.%) and RA330® (Fe-19Cr-35Ni-1.2Si, in wt.%), were evaluated – and compared to AISI 304 – before and after low-temperature triode plasma nitriding (TPN) at 400°C and 450°C. A nitrogen interstitially-supersaturated expanded austenite layer (γ_N) was introduced for all three ASSs after TPN treatment at 400°C, which leads to a) an approximately 4-fold increase in surface hardness, b) a reduction in specific wear rate of at least 2 orders of magnitude in unlubricated dry sliding, and c) an improved resistance to pitting in 3.5 wt.% NaCl aqueous solution. A large number of 'linear defects' (identified in TEM studies as strips of HCP-ε_N) were seen in the γ_N-AG17 layer, that correlate to a comparatively higher surface hardness and better wear resistance. Several slip/shear bands were also seen in the γ_N-330 layer, where local Cr-segregation could occur, that leads to localised corrosion. More importantly, after TPN treatment at 450°C, alloys AISI 304 and AG17 presented a deterioration in corrosion performance, but good corrosion performance was maintained for alloy RA330. Redistribution of Si (in preference to Cr) was revealed in γ_N-330 after TPN treatment at 450°C, whereby Si-alloying at a significantly higher level than the other two alloys investigated appears (in addition to the high Ni content in alloy 330) to be beneficial in delaying CrN precipitation and thus in maintaining the good corrosion performance of γ_N after nitriding at low-to-intermediate temperatures.

1. Introduction

Austenitic stainless steels (ASSs) are a popular class of engineering metal alloys that satisfy an extensive list of applications owing to their excellent corrosion resistance, good weldability and ease of formability, but their wear performance is typically poor [1, 2], which imposes limitations for these types of material in tribological applications. Plasma thermochemical diffusion treatments involving carbon and/or nitrogen have been studied and applied for many years now, as surface engineering methods to improve the poor wear performance of ASS [3-5], with nitriding in particular providing significantly higher hardness and superior wear resistance in sliding and abrasion. Although Cr-nitride formation (and consequent Cr-depletion of the matrix) at high nitriding temperature results in a loss of corrosion performance, nitriding treatments at low-to-intermediate temperatures (typically $\leq$ 450°C) are able to provide sufficient protection for enhanced sliding wear performance without deterioration (and in some cases improvement) of the corrosion performance of ASSs [3, 6-8]. When subjected to the inward diffusion of nitrogen at such treatment temperatures, the surface of ASSs can accommodate nitrogen atoms interstitially up to 38 at.% N under paraequilibrium conditions [9] (cf. equilibrium N solubility of <0.65 at.% [10]) in AISI 316 ASS, generating "colossal supersaturation" [11, 12], and forming a surface layer of nitrogen-expanded austenite (γ_N) known also as 'S-phase' (S_N) [3, 10, 13-16].

Li and Bell [5, 6] reported that, after active screen plasma nitriding of AISI 316 ASS at 420°C, the γ_N layer produced exhibited remarkably enhanced wear resistance under dry sliding – and improved corrosion properties in NaCl aqueous solution. Apart from the widely investigated AISI 304 (Fe-18Cr-8Ni, in wt.%) and AISI 316 (Fe-18Cr-11Ni-3Mo, in wt.%) ASSs, there are a wide variety of other candidate ASSs that may be

74 treated by thermochemical diffusion. In particular Ni, as an expensive austenite-
75 stabiliser in ASS, can be replaced by Mn (either wholly, or in part), to maintain
76 austenitic structure and impart other, beneficial mechanical property modifications –
77 but possibly at the expense of corrosion resistance and high-temperature stability. Ni
78 levels of higher than 8 wt.% can be added to ASSs to improve corrosion resistance (and
79 stability of the austenitic phase), but the tendency towards work hardening under
80 mechanical loading may consequently be reduced. The latter point is related also to the
81 fact that the relative levels and proportions of Ni/Mn in ASS substrates can influence
82 the stacking fault energy (SFE) of austenite, and thereby lead to different plasticity
83 mechanisms in the treated surface layer under interstitial-induced deformation resulting
84 from low-temperature nitriding [17]. In recent work comparing three ASSs, micro-
85 cracks were seen in the face-centred cubic nitrogen-expanded austenite (FCC-γ_N) layers
86 synthesised on a high-Ni ASS [17] – implying a reduced ability to accommodate
87 plastically the internal stresses raised by interstitial nitrogen supersaturation.
88 Importantly (and in contrast to the "mono-phased" FCC-γ_N layers synthesised on AISI
89 316 and other Ni-stabilised ASSs), a hexagonal-close-packed martensitic phase (HCP-
90 ε_N) is revealed within FCC-γ_N layers formed on high-Mn ASSs [17-20], which most
91 likely occurs via SFE-dependent plasticity mechanisms [17, 18]. Although low-
92 temperature plasma nitriding can induce nitrogen interstitial supersaturation in both Ni-
93 free high-Mn ASSs [17, 21] and high-Ni ASSs ([17, 22]), the treatment layers obtained
94 will almost certainly possess different microstructures and properties. In this study, the
95 wear and corrosion performance of a N-containing high-Mn ASS (Fe-17Cr-20Mn-0.5N)
96 and a Si-containing high-Ni ASS (Fe-19Cr-35Ni-1.2Si) were investigated after triode-
97 plasma nitriding treatment (TPN) at two different temperatures below, and near to, the
98 boundary of expected destabilisation of the γ_N formed during TPN treatment, and their

99 treatment responses are compared – both to each other, and to an AISI 304 reference
100 alloy.

101 **2. Experimental procedure**

102 Alloy compositions are shown in **Table 1**. Triode plasma nitriding (TPN) treatments
103 were carried out at 400°C and 450°C for 20hrs in 0.4Pa N_2 + Ar atmosphere (70%
104 partial pressure of N_2 and 30% partial pressure of Ar) using a direct-current triode
105 plasma configuration in a modified Tecvac IP70L triode plasma-assisted PVD coating
106 unit [15, 23, 24]. Sample preparation methods and the TPN treatment process are both
107 described in detail in Ref. [17]. The untreated and TPN-treated samples were
108 characterised and evaluated under ball-on-plate reciprocating-sliding wear and
109 potentio-static/-dynamic corrosion testing. All untreated samples before were polished
110 to a mirror surface finish (Ra ~ 0.02 μm) before TPN treatment. Post-treatment X-ray
111 diffraction analysis (XRD) was performed in Bragg-Brentano geometry using Bruker a
112 D2 PHASER diffractometer (30 kV, 10 mA, Cu-Kα 0.15418 nm). The X-ray
113 attenuation depths (~95% of signal) for Bragg conditions were estimated (using
114 AbsorbDX software) as being ~2-5 μm over a 2-theta range of 30-100°, based on the
115 compositions of the stainless steels prior to TPN treatment. Scanning electron
116 microscopy (SEM) and Energy Dispersive X-ray (EDX) spectroscopy were performed
117 via a Philips XL30S instrument and a Jeol 7000F instrument (both with Oxford
118 Instruments EDX system attached). Optical images were obtained from a Nikon Eclipse
119 LV150 Optical Microscope (OM) equipped with Buehler Omni Met software. High
120 angle annular dark field (HAADF) imaging and EDX analysis were also performed
121 under scanning transmission electron microscopy (STEM) using an FEI Philips Tecnai
122 F20 instrument (FEG, 200 kV).

123

124 **Table 1.** Material compositions, in wt.%

Material	ASTM	Code	Fe	Cr	Ni	Mn	N	Others
AISI 304[a]	ASTM A240	304	Bal.	18.2	8.1	1.7	0.1 max	0.07C max, 0.3Si
Staballoy® AG17[b]	– – –	AG17	Bal.	17.4	0.8	18.9	0.5	0.6Co, 0.3Si
RA330®[c]	ASTM B536-07	RA330	Bal.	18.5	34.9	1.4	0.01	0.16Al, 0.14Ti, 0.11Cu, 1.2Si, 0.05C

125 [a] Composition of AISI 304 was confirmed under EDX analysis, with expected
126 maximum nitrogen and carbon content taken from ASTM A240.
127 [b] Composition of Staballoy® AG17 was confirmed under EDX analysis, with nitrogen
128 content specifically determined via chemical composition analysis performed by
129 Sheffield Assay Office
130 [c] Composition of RA330® was based on chemical composition analysis by the material
131 supplier (NeoNickel, Blackburn, UK), with the content of main alloying elements
132 confirmed under EDX analysis.

133

134 Material surface microindentation hardness was evaluated with a Struers Durascan 70
135 hardness tester (using Vickers indenter geometry, 0.025kg load and 15s dwell time).
136 Unlubricated (dry) sliding wear performance was evaluated using a proprietary
137 reciprocating-sliding tribometer at a frequency of 8 Hz with a reciprocation amplitude
138 of ±5 mm (i.e. 20 mm stroke). A 10 mm diameter WC-Co ball (supplied by Spheric-
139 Trafalgar Ltd.) was loaded at ~9.8 N and worn against untreated/TPN-treated sample

surfaces for 500 m. The maximum initial (static) Hertzian contact stress for a 10 mm WC-Co ball loaded against untreated ASS substrate is in this case estimated to be ~1.27 GPa. Before each test, sample and ball were ultrasonically cleaned and rinsed with isopropanol for 10 mins, and dried using dry compressed air. All sliding tests were performed under ambient conditions (within an ambient temperature range of ~18-27°C and at relative humidity between 15 and 25%). At least two repetitions of each sliding test were performed, with wear scars evaluated using a mechanical stylus profilometer (Veeco Dektak 150 instrument) with 25µm diameter hemispherical diamond tip.

The electrochemical cell employed for corrosion performance evaluation was equipped with a Saturated Calomel reference electrode (SCE, $Hg/HgCl_2$ – sat. KCl) and a platinum counter electrode. The treated sample surface with an exposure area of ~0.79 cm^2 (as the working electrode) was first immersed in 3.5 wt.% NaCl solution for 3600s to establish a stable open circuit potential (OCP) and then potentiodynamically polarised from -1 V to +2 V at a scan rate of 1.67 mV/s. A proprietary Scribner Associates / Solartron CorrWare® software was used for corrosion process monitoring, data collection and analysis.

3. Results and discussion

3.1 Surface characterisations

Before TPN treatment, untreated ASSs all presented FCC-γ XRD peaks (**Fig. 1**). Alloy RA330 was received in the solution annealed state, such that all FCC-γ XRD peaks were observed. However, it is worth mentioning that the high peak intensity of γ(220) on untreated alloy 304, and the absence of γ(200) and γ(311) peaks on untreated AG17,

suggest different degrees of texture for these two ASSs, probably owing to previous mechanical processing steps. In addition, a small peak at ~44.5° for untreated 304 in **Fig. 1** suggests the presence of some deformation-induced α′ martensite, created at the near-surface during sample grinding/polishing.

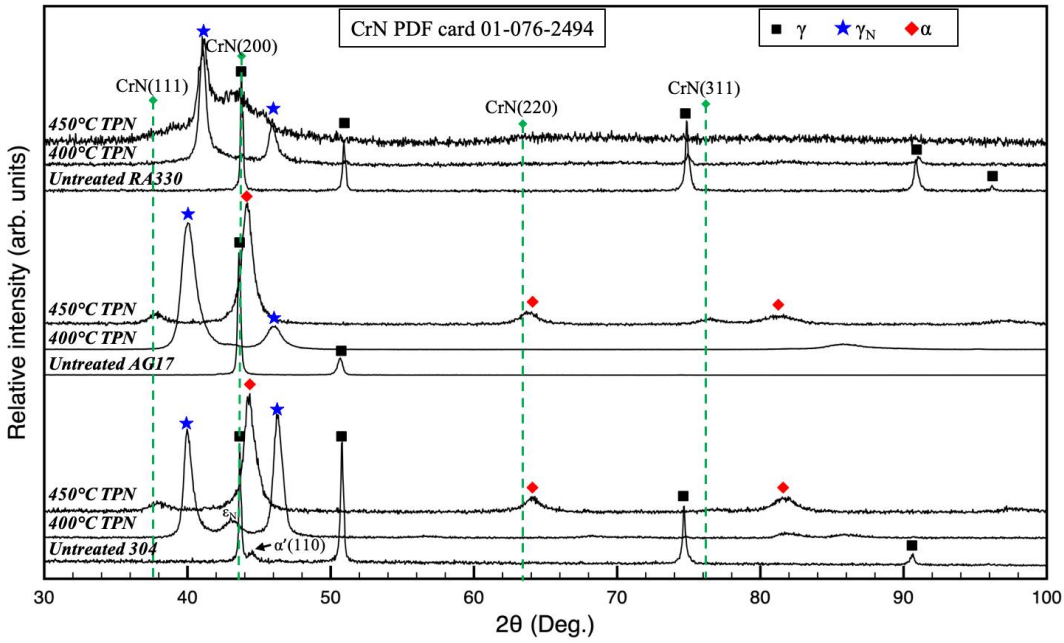

Fig. 1 XRD profiles for AISI 304, Staballoy® AG17 and RA330® before and after TPN treatments at 400°C and 450°C for 20hrs

Characteristic anisotropic shifting of XRD peaks to lower angles of 2θ is observed for 400°C TPN-treated ASSs in **Fig. 1**, indicating formation of γ_N expanded austenite on all three ASSs. Nevertheless, a large number of 'lines' were also observed, either parallel to or interwoven with each other, in the γ_N layer on AG17 after TPN treatment at 400°C (**Fig. 2a, b**). TEM investigations revealed that these 'lines' in γ_N are in fact strips of HCP-ε_N, that follow the Shoji-Nishiyama-structure-orientation relationship, i.e. $<110>\gamma_N$ //$<2110>\varepsilon_N$ and $\{111\}\gamma_N$ //$\{0001\}\varepsilon_N$, and are most likely present as a result of transformation-induced plasticity (TRIP) occurring under interstitial-supersaturation induced deformation [17, 18]. A similar layer morphology (of ε_N strips embedded

180 within γ_N) could be traced back to the early expanded-austenite work of Hannula et al.
181 [14] and has also been revealed on AISI 202, AISI 304 and AISI 316L after plasma
182 nitriding [19, 20, 25]. It is worth mentioning that a small peak at ~43.1° was also seen
183 for 400°C TPN-treated AISI 304 (as indicated in **Fig. 1**), which could be attributed to
184 the presence of some ε_N nanostructuring within γ_N-304 as well (see also Refs. [19, 26]).
185
186 Notably, the number density of HCP-ε_N strips is not uniform in the γ_N layer (**Fig. 2a**).
187 The variation in number density of HCP-ε_N regions can be attributed to the different
188 levels of interstitial-induced deformation for the onset of TRIP effects in γ_N [17, 18].
189 Although not seen in **Fig. 1**, HCP-ε_N peaks were revealed under GAXRD analysis [18],
190 where a shallower (and narrower range of) X-ray attenuation depth is achieved (i.e.
191 ~0.4-0.6 μm, compared to the previously mentioned ~2-5 μm under conventional
192 Bragg-Brentano XRD). This is clearly due to the larger number density of HCP-ε_N
193 strips at the near surface, where the highest absorbed nitrogen content occurs. In
194 addition, as indicated in **Fig. 2a**, the number of HCP-ε_N strips varies between different
195 metallurgical grains of different crystallographic orientation within the γ_N layer.
196 Considering the anisotropic deformation/expansion behaviour for FCC ASSs under
197 nitrogen interstitial supersaturation [27-29], it is perhaps not surprising that the level of
198 interstitial-induced deformation (and consequent) HCP-ε_N number density is dependent
199 on grain orientation.
200
201 No obvious segregation of Fe, Cr or Mn was seen across the HCP-ε_N strips under SEM-
202 EDX (**Fig. A1** in **Appendix A**). The signal variation in nitrogen-mapping under SEM-
203 EDX analysis (**Fig. A1**) for HCP-ε_N strips is believed to be due to the topography
204 obtained after etching, because no significant variation in N concentration was observed

205 across HCP-ε_N strips under STEM-EDX analysis (where the region of inspection was
206 on a rather flat TEM thin foil) [18]. However, although hardly found in γ_N-AG17, low-
207 Fe/high-Cr regions were occasionally observed at grain boundaries (**Fig. A1** in
208 **Appendix A**), accompanied by a large number density of ε_N strips in the adjacent γ_N
209 grain. Cr-segregation at such a low treatment temperature might be facilitated by the
210 high defect density at a grain boundary, or by the intersection between ε_N strips and
211 grain boundaries. Note also that – whereas **Fig. A1** highlights an example of an isolated
212 local region that exhibits such Cr-segregation – most of γ_N-AG17 shows a rather
213 homogenous elemental distribution.
214
215 Corresponding to the thick and dark top layer shown in **Fig. 3a**, CrN and α peaks could
216 be identified for AG17 after TPN treatment at 450°C (**Fig. 1**), for which TEM
217 investigations previously showed cellular Cr + α, with an interlamellar spacing of ~1-
218 3 nm [17]. Nevertheless, bright islands – although small in size – can still be seen within
219 the topmost dark layer (inset in **Fig. 3a**), suggesting regions of residual γ_N. Electron
220 diffraction patterns also revealed a diffraction halo between the CrN(111) and α-Fe(110)
221 diffraction rings [17], that hints at residual γ/γ_N even in the decomposed regions. The
222 decomposition is 'incomplete'; a rather small CrN peak is seen therefore in **Fig. 1**, since
223 not all Cr is transformed to CrN. With increasing treatment temperature (or prolonged
224 treatment time), the decomposition microstructure would approach thermodynamic
225 equilibrium, such that CrN XRD peaks (as shown in **Fig. 1**) may increase in intensity
226 and become sharper (as demonstrated in Ref. [22]). Below the topmost layer, there is
227 an underlying layer on 450°C TPN-treated AG17 that is believed to be residual un-
228 decomposed γ_N (as indicated in **Fig. 3b**). Notably, the topmost layer is too thick (~16.1

μm) for any γ_N peaks from the underlying layer to be detected by the XRD analysis presented in **Fig. 1**.

In contrast, a bright treatment layer was seen in the high-Ni RA330 alloy surface after TPN treatment at both 400°C (**Fig. 2c**) and 450°C (**Fig. 3c**). Compared to the γ_N-AG17, similar 'linear' sub-features – although much less in number – were seen also inside γ_N-330 (**Fig. 2c, d**) – which are believed to be planar defects, such as shear or slip bands [17, 18]. EDX analysis (see **Fig. A2&A4** in **Appendix A**) suggests Cr segregation at slip/shear bands and at grain boundaries in γ_N-330. Differentiation between slip and shear bands is difficult under SEM-EDX. However, given the high dislocation density and intense plastic deformation at shear bands, it is anticipated that Cr-segregation is more likely to occur at shear bands, compared to slip bands. The slip/shear bands and grain boundary regions in γ_N-330 appear rather 'thick' at 450°C (**Fig. 3c**), a phenomenon that could be associated to local Cr-segregation (**Fig. A4**) and/or micro-cracking under high residual stress.

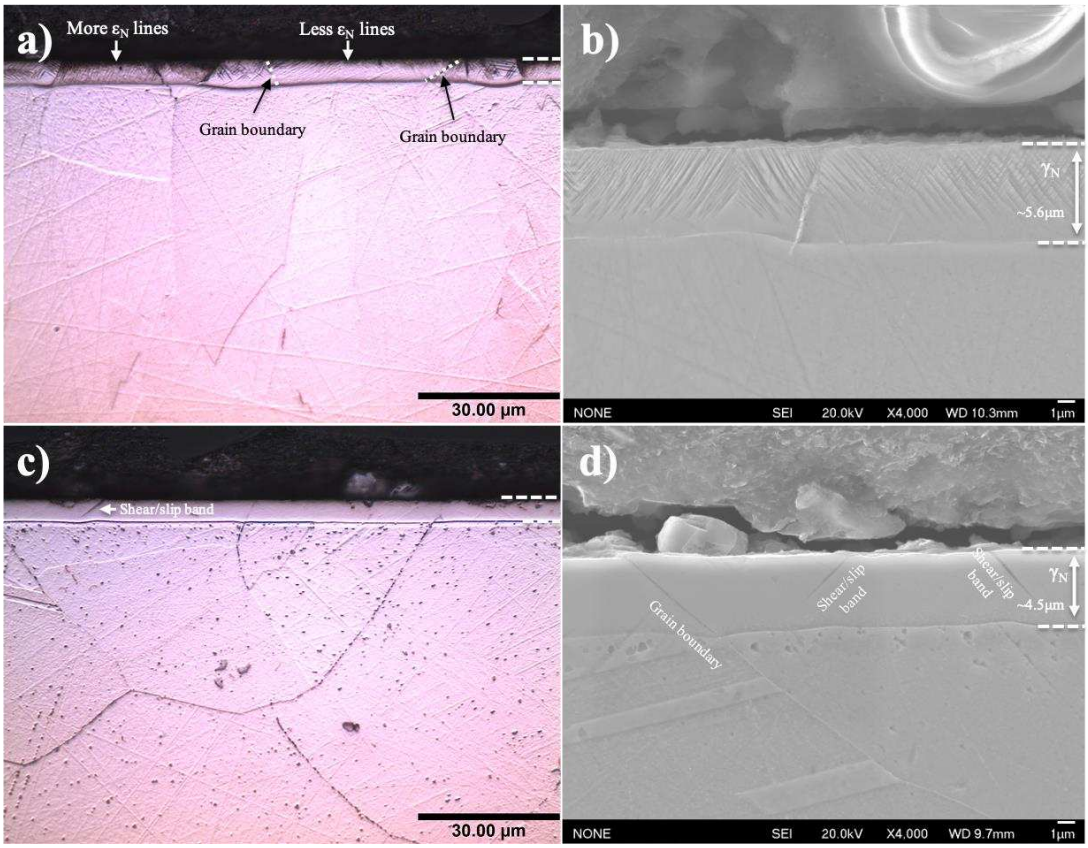

Fig. 2 OM and SEM images showing the treatment layers on AG17 (a, b, respectively) and RA330 (c, d, respectively) after TPN treatment at 400°C for 20hrs (etched in 50HCl-25HNO_3-25H_2O; vol%); see **Fig. A1&A2** in **Appendix A** for SEM-EDX maps.

No clear CrN XRD peak can be seen in **Fig. 1** for alloy RA330 TPN-treated at 450°C. However, spheroidal (semi-)coherent nano-precipitations were seen within γ_N grains and incoherent crystalline decomposition products were evident at grain boundaries under TEM analysis [17]. Considering the high Cr content, the observed 'nano-precipitations' were attributed to CrN formation in γ_N and a decomposition mechanism of γ_N-330 → CrN + γ was proposed for the crystalline nano-phases at grain boundaries [17]. Given the strong chemical affinity between Al/Ti (both ≤0.2 wt.% in RA330) and nitrogen, it is also thought that the CrN nano-precipitates could contain Al/Ti. Similar decomposition mechanisms were also reported for various Ni superalloys after gaseous nitriding at 400-440°C (depending on substrate composition) [30].

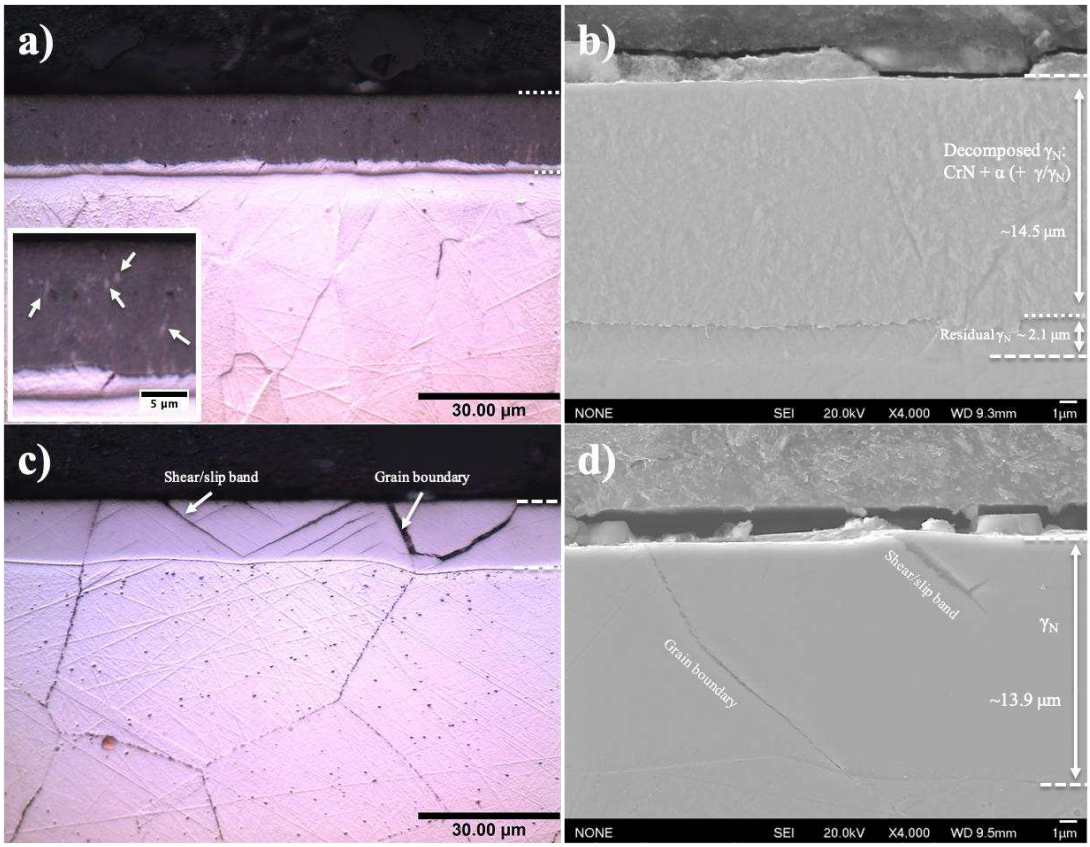

Fig. 3 OM and SEM images showing the treatment layers on AG17 (a, b, respectively) and RA330 (c, d, respectively) after TPN treatment at 450°C for 20hrs (etched in 50HCl-25HNO_3-25H_2O; vol%); see **Fig. A3&A4** in **Appendix A** for SEM-EDX maps

However, further STEM-EDX investigations carried out in the present study revealed, intriguingly, re-distribution of Si (in preference to Cr) in γ_N-330 for RA330, after TPN treatment at 450°C for 20hrs (**Fig. 4**). While the Si-rich regions appear to be depleted in Fe (**Fig. 4b**) and Ni (**Fig. 4d**), **Fig. 4c** suggests a rather homogenous distribution of Cr between the Si-rich regions and the γ_N matrix. Additionally, the Cr-containing Si-rich phase presents a slightly stronger N-signal to the (still high-N) γ_N-330 matrix (**Fig. 4e**), in which case these spherical particles could possess a nitrogen content higher than ~25 at.% (as measured 'globally' from the treated near-surface under SEM-EDX). Given the electron diffraction pattern and the diffraction distance ratio of 1.10 (cf. ~1.09

for CrN and γ_N-330) [17], these Si-rich regions are most likely (semi-)coherent (Cr, Si)$_x$N nanoprecipitates that could be a pre-cursor to (Si-containing) CrN formation. Since no substantially new XRD peaks were seen in **Fig. 1**, (Cr, Si)$_x$N might be a paraequilibrium phase to CrN, where a significant fraction of the Cr atoms are substituted by Si. The intermediate decomposition mechanism for γ_N-330 can thus be tentatively identified as being: γ_N-330 → (Cr, Si)$_x$N + (low-Si, lower-N) γ_N, during TPN at 450°C for 20hrs. No significant local variation in Al, Ti and Cu distribution can be seen in **Fig. 4**, but this could be due to their small elemental concentrations in the alloy. However, considering their strong chemical affinity for nitrogen, the proposed (Cr, Si)$_x$N phase might also contain some Al and Ti. A STEM-HAADF image presented in **Fig. A5, Appendix A** shows (at slightly lower magnification) the random distribution of such nanoprecipitations. After seeing such morphology for the whole TEM sample (covering a depth of ~5.5 μm [17]), it is anticipated that this nanoprecipitation occurred across the entire γ_N-330 layer produced at 450°C.

The sluggish decomposition of alloy RA330 was previously correlated to high-Ni content and high material SFE [17]. However, the work presented here reveals for the first time that the significant Si alloying in this alloy is most probably contributing to the good thermal stability of γ_N-330 under TPN treatment as well – despite the known α-stabilising characteristics of this element according to Schaeffler diagram [31]. Christiansen et al. [32] argued that additions of Al and Ti in ASS (as strong nitride/carbide forming elements) could compete against and suppress the formation of CrN in nitrogen-expanded austenite. Compared to those 'conventional' strong-nitride-forming elements, Si is a small substitutional metalloid atom and would arguably be expected to be more mobile than other (metallic) substitutional elements at the chosen

nitriding temperatures (~400-450°C), thus localised Si segregation could be (more) efficient in delaying CrN formation in γ_N layers fabricated at low-to-intermediate treatment temperatures. Intriguingly, instead of a "binary" silicon nitride that competes against CrN formation, a Cr-containing compound is formed. Importantly, these finely-dispersed nano-precipitates most likely form nitrogen reservoirs that drain interstitial nitrogen from the interstitially-supersaturated matrix and 'relax' the chemical potential for Cr-segregation, postponing decomposition of γ_N.

While being a commonly-used alloying element in many steels (for various metallurgical purposes), Si (of ~1.2 wt.%) is most likely added to alloy RA330 primarily for the purpose of improving high temperature oxidation and scaling resistance – and also to control carburization in high-temperature carbon-rich combustion atmospheres. As **Table 1** attests, both AISI 304 and AG17 contain 0.3 wt.% Si – but the 4-fold higher Si content in alloy RA330 seems to yield a benefit that is not generated in the other alloys. This work reveals that (at some yet-to-be-determined threshold level) Si could also be an effective alloying element to inhibit Cr-nitride formation for ASSs during low-to-intermediate temperature nitriding, creating the potential for higher treatment temperatures to be applied to such an alloy (without significant loss of corrosion performance) – effectively permitting thicker diffusion layers and/or shorter treatment times to be implemented. There is clearly a requirement for further comparative studies on certain commercially-available 'high temperature' ASSs [33], that contain a range of Cr, Ni and Si contents ranging between (and beyond) those of 304 and 330, such as the widely-available, similar (but not 'identical') Si-containing AISI 309/310. However, as mentioned above, Si is also a known ferrite stabiliser, e.g. Si addition higher than ~2 wt.% in AISI 304 could lead to ferrite

formation [34]. Most commercial high-Si ASSs (e.g. Sandvik SX®) are 'incomparable' to the common AISI 304/316 ASS grades for future nitriding studies, because high Ni content (and/or extra Cu addition) is often utilised to compensate for the α-stabilising propensity of high-Si addition. For a comprehensive picture of the real benefit of Si-alloying in delaying the decomposition of γ_N – and whether (for example) some higher minimum Ni-content is also needed, one may need to make 'bespoke' compositions, composed of a low-Ni and high-Ni group, both at a similar Cr level (e.g. ~18 wt.%) but with Si contents in a range from the 'normal' 0.3 wt.% Si upwards, allowing comprehensive inter-comparisons to be made, on the influence of each incorporated element on phase stability.

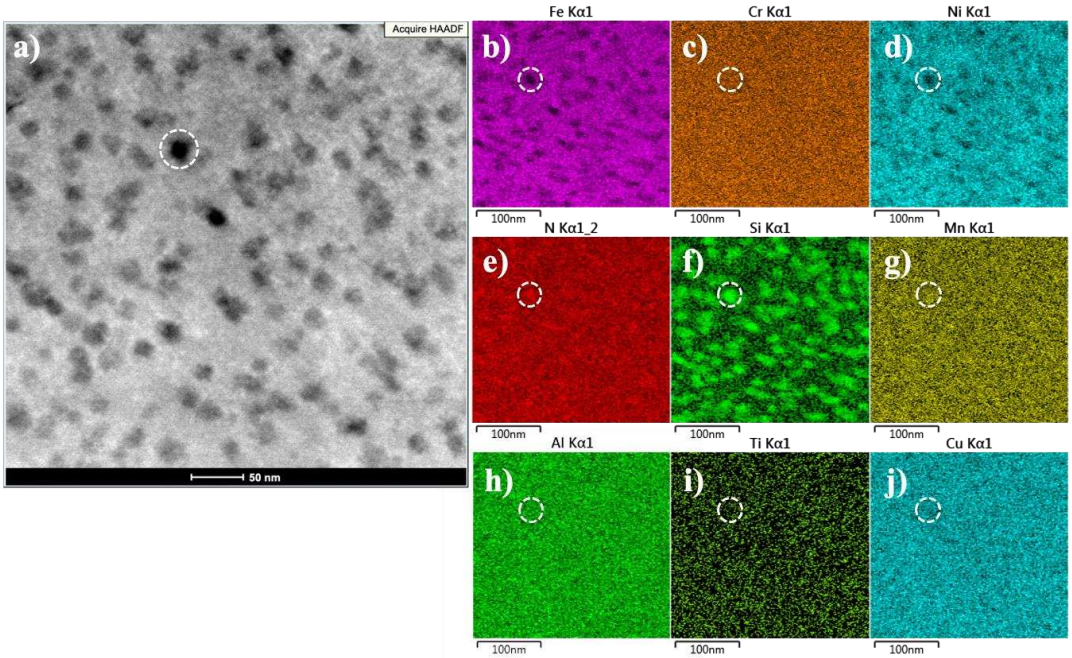

Fig. 4 a) HAADF-STEM for the surface of alloy RA330 after TPN treatment at 450°C, and STEM-EDX maps for b) Fe, c) Cr, d) Ni, e) N, f) Si, g) Mn, h) Al, i) Ti, and j) Cu. A Si-rich region is highlighted in the dashed circle to aid viewing. Note that the element maps in **Fig. 4b-j** do not perfectly superimpose with the HAADF image in **Fig. 4a**, because of sample drift during prolonged EDX scan.

The surface nitrogen contents in all three ASSs are extremely high (exceeding 20 at.%) after TPN – and are listed in **Table 2**. It is worth mentioning that the SEM-EDX data should be considered as being only semi-quantitative, especially for light elements such as nitrogen. Nevertheless, several clear trends can be seen and are discussed below. Firstly, the measured surface nitrogen content reduces from high-Mn to high-Ni content for the three ASSs investigated here (each being at a similar Cr level of ~18 wt.%), an effect that might be associated to increasing nitrogen solubility at higher Mn-content (and conversely with higher Ni-content). Secondly, a significant drop in surface nitrogen content was seen with increasing treatment temperature from 400°C to 450°C in alloys AISI 304 and AG17 (**Table 2**), which hints at higher nitrogen solvency under "colossal (interstitial) supersaturation" [11, 12] at the lower treatment temperature, than in the (partially decomposed) microstructures generated at the higher temperature – presumably owing to the low nitrogen solvency in the (Cr-depleted) α matrix after Cr-nitride precipitation has commenced. In contrast, the Si-rich nano-precipitates identified in 450°C TPN-treated RA330 (**Fig. 4**) correlate to a slightly higher surface nitrogen content, compared to the 400°C TPN-treatment of the same alloy.

Table 2. Surface nitrogen contents, Vickers hardness, specific sliding wear rates, and wear depths (after sliding for 500 m) for the three ASSs investigated. Values are presented as mean ± standard deviation.

Materials	**Treatments**	**Surface nitrogen content, at. %**	**Vickers hardness, $HV_{0.025}$**	**Specific sliding wear rate, mm^3/Nm**	**Sliding wear depth, µm**
304	Untreated	/	235 ± 10	$1.2 \pm 0.1 \times 10^{-4}$	51.6 ± 4.7
	TPN at 400°C	26.9 ± 0.9	1325 ± 63	$4.8 \pm 1.8 \times 10^{-7}$	1.1 ± 0.3
	TPN at 450°C	19.2 ± 0.5	1656 ± 67	/	/
AG17	Untreated	(1.9*)	419 ± 9	$1.4 \pm 0.2 \times 10^{-4}$	62.5 ± 4.1

	TPN at 400°C	34.4 ± 0.3	1808 ± 57	$1.3 \pm 0.5 \times 10^{-7}$	0.7 ± 0.1
	TPN at 450°C	29.2 ± 0.4	2053 ± 97	/	/
RA330	Untreated	/	210 ± 7	$2.7 \pm 0.5 \times 10^{-4}$	91.1 ± 7.6
	TPN at 400°C	24.0 ± 1.1	1048 ± 109	$12.5 \pm 4.2 \times 10^{-7}$	3.0 ± 0.6
	TPN at 450°C	25.1 ± 0.8	1573 ± 33	/	/

*The ~1.9 at.% N is for the untreated alloy AG17, that was specifically determined via chemical composition analysis

3.2 Surface hardness and dry sliding wear performance

Material surface micro-indentation hardness values, specific sliding wear rates and wear depths are shown in **Table 2**. Material surface hardness and wear rates are plotted in **Fig. 5**. All TPN-treated surfaces were hardened to above 1000 $HV_{0.025}$. The average layer thicknesses of TPN-treated alloys AG17 and RA330 were averaged from 50 cross-sectional measurements on etched sample cross-sections, being ~5.3 μm and ~4.3 μm respectively at 400°C; and ~18.5 μm and ~13.8 μm respectively at 450°C [17]. The indentation depths of TPN-treated alloy AG17 and RA330 were estimated as being ~0.7 μm and ~1.0 μm respectively for 400°C treatments – and ~0.7 μm and ~0.8 μm respectively for 450°C. For the 400°C TPN-treated surfaces, the highest surface hardness was measured at ~1808 $HV_{0.025}$ on alloy AG17, and the lowest hardness value at ~1048 $HV_{0.025}$ was found for γ_N-330. The high surface hardness of 400°C TPN-treated AG17 appears to correlate well to the presence of HCP-ε_N in the treatment layer. However, the enhancements in hardness for both of the special ASSs originate from a combination of solid solution strengthening and strain hardening (with different SFE-dependent plasticity mechanism involved) under different levels of nitrogen supersaturation. The superior hardness enhancement for AG17 could eventually be attributed to the different hardening mechanisms at a higher nitrogen absorption level, for which HCP-ε_N is a consequence (rather than a cause). Additionally, although

indentations depths were shallower than the layer thickness of γ_N at 400°C, indents are supported by the entire treatment layer and the unmodified core. Thus, a higher substrate hardness also contributes to a higher measured surface hardness for AG17 after TPN at 400°C. Given the significantly deeper layers generated at 450°C, measured surface hardnesses at this temperature are believed to be independent of the unmodified core values. The further increase in surface hardness with treatment temperature from 400°C to 450°C can be attributed to an increase in layer thickness and could also be attributed to the formation of hard non-metallic precipitates.

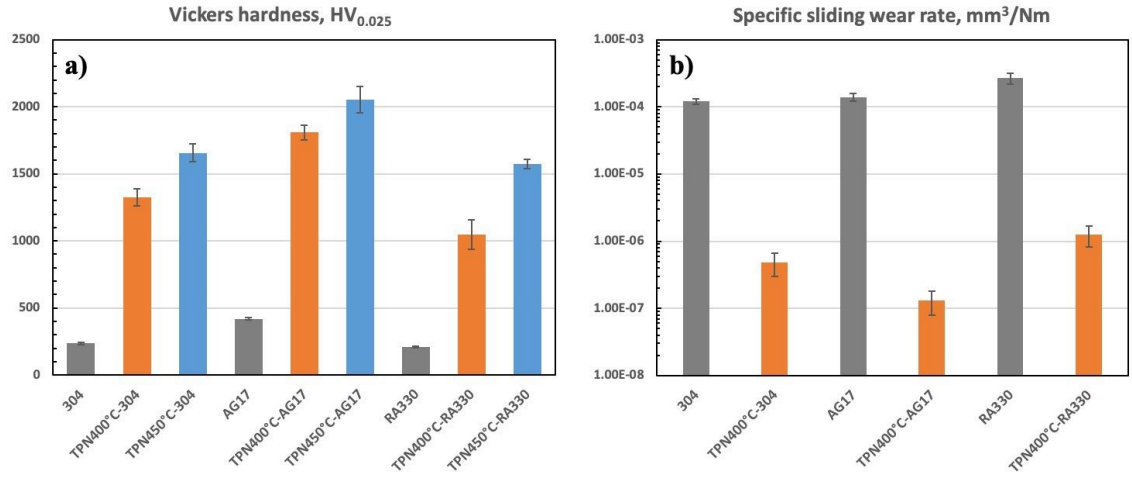

Fig. 5 Bar charts showing a) material surface hardness and b) specific sliding wear rate before and after TPN treatments

Since decomposition of γ_N at high treatment temperature is known to damage the corrosion performance of ASSs (making them unfit for corrosion applications), the sliding wear performance evaluation in this study focus on the γ_N layers synthesised at 400°C. Compared to the untreated substrates, no significant change in friction coefficient was seen for all three ASSs after TPN treatments at 400°C (**Fig. B1** in **Appendix B**). However, the measured wear rate was reduced by around two to three orders of magnitude (from approximately 100-300 × 10^{-6} mm^3/Nm, to 0.1-1.3 × 10^{-6} mm^3/Nm) and the measured wear depth was correspondingly reduced by at least 94%

403 (from ~50-90 μm to ~0.7-3.0 μm) (**Table 2**). The reductions in surface wear rate after
404 TPN treatment were in fact ~99.6% on alloy AISI 304, ~99.9% on high-Mn alloy AG17
405 and ~99.5% on high-Ni alloy RA330. Given the wear depth of ~0.5-3 μm (**Table 2**)
406 and the treatment layer depth of ~4-6 μm, none of the treatment layers were penetrated
407 in the 500m sliding tests. As reported for other typical ASSs (such as AISI 316 ASS
408 [4]) after plasma nitriding, the improvement in dry sliding wear resistance in this study
409 can be attributed to enhanced load-bearing capacity, reduced plastic deformation and
410 adhesive wear, all of which can be correlated to nitrogen supersaturation levels (and
411 associated increases in surface hardness). Consistent with the trends of surface hardness,
412 the enhancement in wear resistance also increases noticeably from high-Ni to high-Mn
413 ASS (**Fig. 5**).
414
415 The wear mechanisms for both of the untreated proprietary ASSs are characterised by
416 adhesive (galling) and abrasive wear. Abrasive grooves and wear products were seen
417 on the wear tracks on alloy AG17 (**Fig. 6a**) and RA330 (**Fig. 7a**). EDX spectra of the
418 wear tracks on both untreated ASSs indicate the presence of oxygen (**Fig. 6d**, **Fig. 7c**).
419 No trace of W or Co from the ball counterface could be identified on untreated ASSs
420 after sliding. In addition, the 'oval-shaped' attachments on top of the WC-Co ball
421 counterface (see **Fig. B2** in **Appendix B**) indicate that wear damage occurred mainly
422 on the untreated ASS surfaces. It appears that wear debris from ASSs are oxidised and
423 attached onto the surface of the stainless steel samples (and also to the ball counterface)
424 during sliding. Note that both the WC-Co balls and ASS samples were immersed in
425 isopropanol and ultra-sonicated for 10 mins before inspection. The firm attachment of
426 oxidised wear products on all worn surfaces suggests oxidative and adhesive wear.
427 Nevertheless, compared to the large amount of (oxidised) wear products on RA330 (**Fig.**

7a, and see also **Fig. B3** in **Appendix B**), less wear products were seen on AG17 (**Fig. 6a**), which indicates less oxidative wear and can be attributed to the high pre-existing level of N in this alloy – whose original design purpose was to provide improved resistance to adhesion and galling in demanding environments (such as the offshore oil & gas extraction industry).

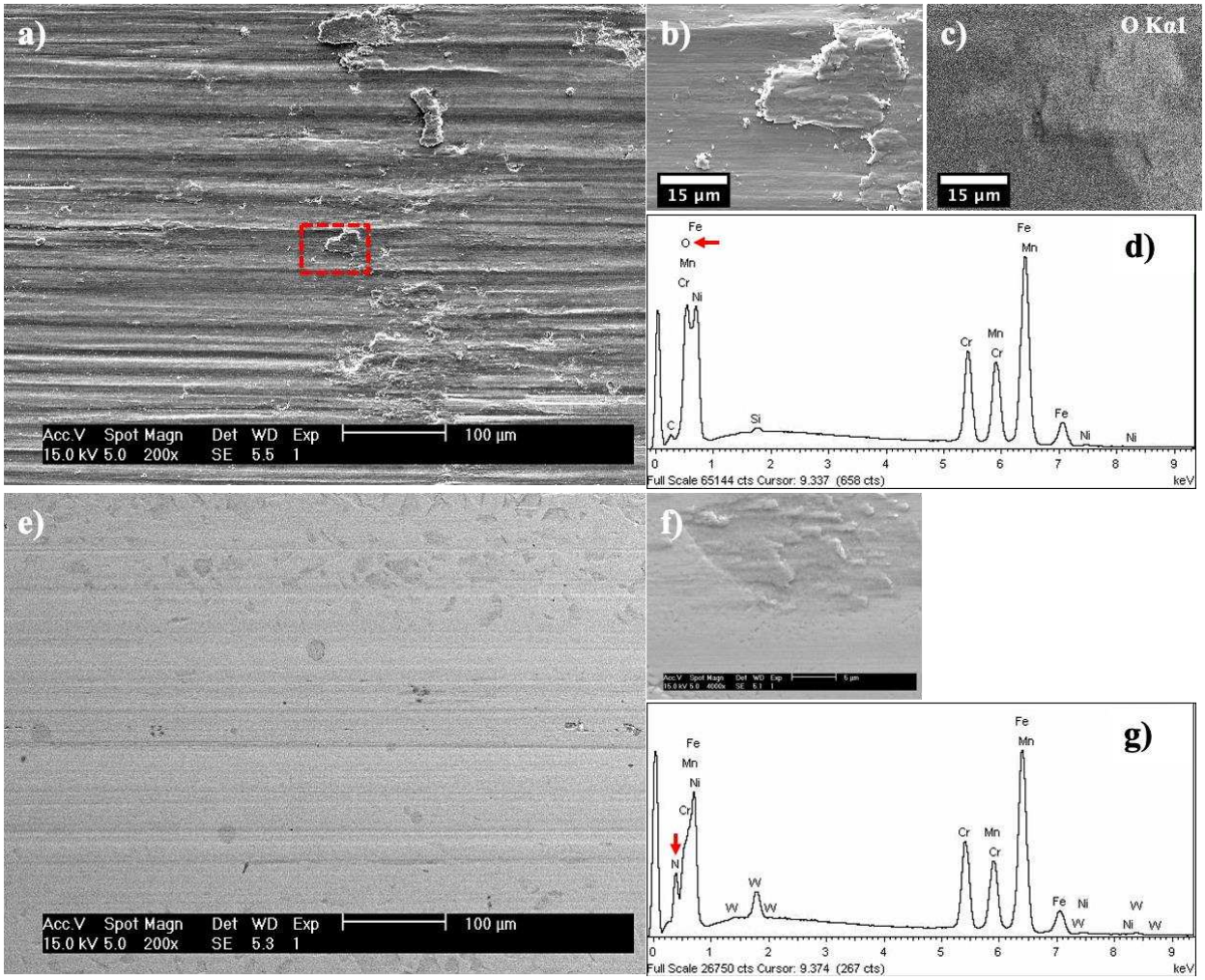

Fig. 6 SEM images showing the morphology of the wear track on a) untreated AG17 and e) 400°C TPN-treated AG17; b) SEM image, c) EDX map for Oxygen, and d) EDX spectrum for a local feature on untreated AG17; f) SEM image and g) EDX spectrum for a local feature on 400°C TPN-treated AG17. Sliding direction is horizontal for all SEM images presented.

441 In contrast to untreated ASSs, the wear tracks on 400°C TPN-treated ASS appear much
442 "cleaner", with a significantly reduced amount of wear products (**Fig. 6e & 7d**), while
443 abrasive wear was still evident. Oxygen was not identified in the EDX spectra for the
444 wear tracks on TPN-treated surfaces (**Fig. 6g** & **7f**). Instead, strong N-Kα peaks are
445 detected (**Fig. 6g & 7f**). One may argue that the adhesive and oxidative wear found for
446 ASSs under dry sliding was significantly reduced after TPN treatment. In addition, W
447 is identified in the EDX spectrum in **Fig. 6g** (for the region shown in **Fig. 6f**), indicating
448 material transfer from the counterface during sliding. After introducing a hard surface
449 layer on ASS via TPN, the WC-Co ball is indeed significantly worn and flattened; for
450 example, the diameter of the flat wear scar on the WC-Co ball is conformal to the wear
451 track on TPN-treated AISI 304 (~580 μm, see **Fig. B2d&h** in **Appendix B**).

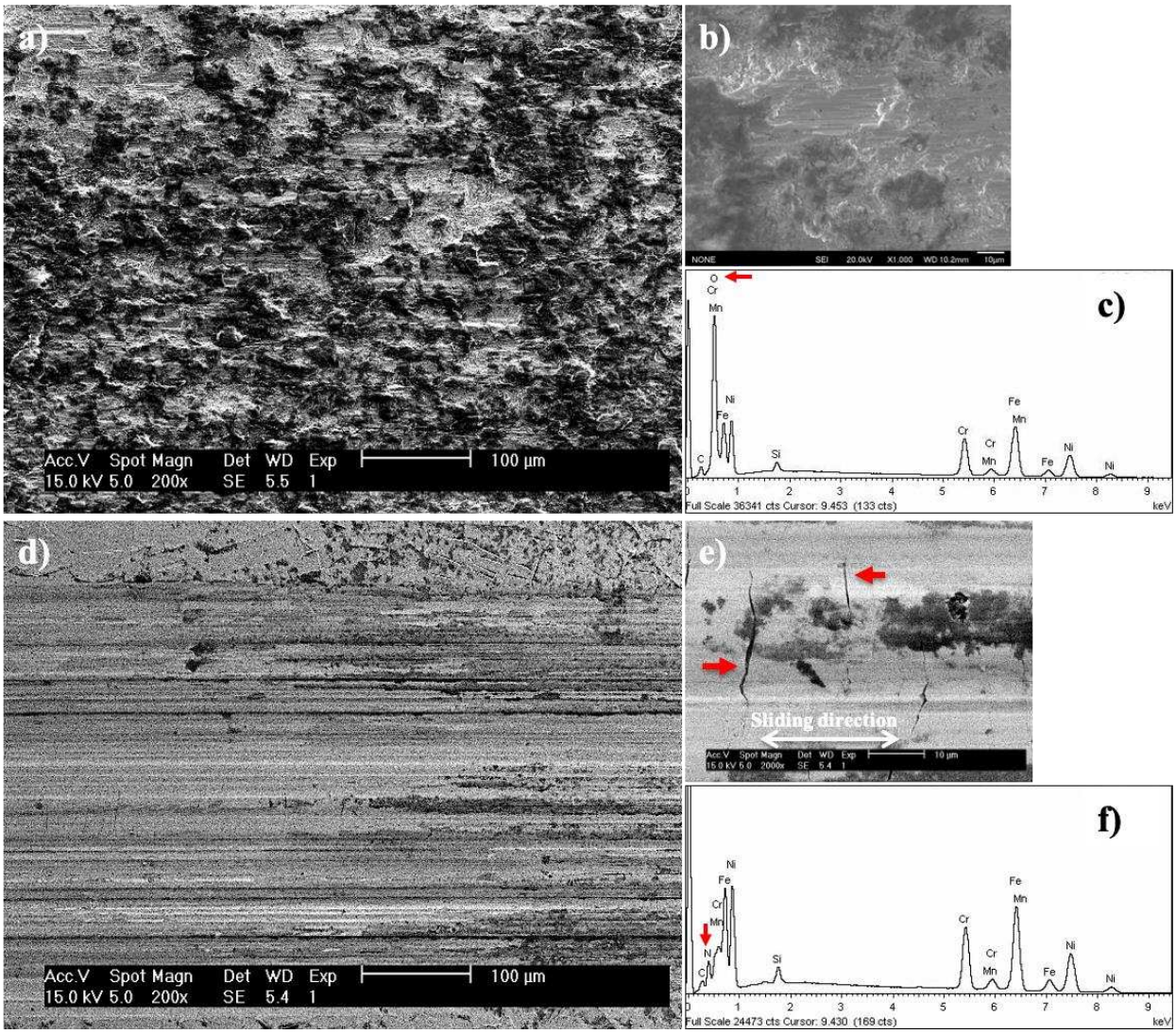

Fig. 7 SEM images and typical EDX spectrum for the wear scars on untreated RA330 (a, b, c, respectively) and 400°C TPN-treated RA330 (d, e, f, respectively) after sliding. Sliding direction is horizontal for all SEM images presented.

More significantly, some parallel micro-cracks were observed, perpendicular to the sliding direction, in the wear track on TPN-treated alloy RA330 (under SEM in **Fig. 7e**, or see OM images in **Fig. B2** in **Appendix B**), but not in those on TPN-treated AG17. These micro-cracks in wear track could be correlated to the poor toughness of the γ_N generated (as discussed previously by many authors [9, 35-38]). Hoeft et al. [36] reported similar cracks, perpendicular to the axial direction, after tensile testing of the γ_N-316 layers synthesised on AISI 316 ASS. Plasma immersion ion implantation (PI^3)

treatments applied at 360°C to 430°C were also reported to reduce the fracture toughness of AISI 316 under tensile testing [36]. Christiansen et al. [39, 40] reported that the γ_N-316 layers synthesised at high nitriding potentials are prone to brittle cracking, and micro-crack networks were observed in γ_N-316 layers at high, but not low, nitriding potentials under gaseous nitriding [9]. The cracks observed in the wear tracks on γ_N-330 may be attributable to high nitrogen uptake under a high nitrogen volume fraction in the treatment chamber (i.e. 70:30 N_2:Ar volumetric ratio) during TPN. To address this issue, one might apply treatments at a lower nitrogen gas volume fraction (such as 30:70 N_2:Ar) during TPN treatments for this material, in order to lower interstitial concentration at the near-surface.

In addition, Hoeft et al. [36] and Christiansen et al. [40] argued that the reduced toughness of γ_N-316 is likely to arise from the combined effects of both high residual stress and high stacking fault (SF) density. However, no evidence of SFs was found in γ_N-330, while SF-mediated HCP-ε_N was observed in γ_N-304 and γ_N-AG17, at ~8 vol.% and ~24 vol.% respectively (based on DF-TEM imaging inside randomly-selected γ_N grains at the near-surface), after TPN at 400°C [17, 41]. The presence of micro-cracks in the wear track on γ_N-330 (but not on alloy AG17) indicates that this layer brittleness issue is not directly associated to SF density, but might be primarily owing to high residual stress levels. Furthermore, γ_N-AG17 apparently showed no obvious 'brittle' features under dry sliding wear. In contrast to the suggestions by Hoeft et al. [36] and Christiansen et al. [40], SF generation in low-Ni (high-Mn) ASSs appears somehow beneficial in reducing the adverse embrittling effects of colossal nitrogen supersaturation. SF-mediated transformation-induced plasticity and localised hardening effects are likely to be key factors, that relax the high residual stress and

counter the brittle failure of supersaturated layers. The brittleness issue seen in the γ_N-330 layer formed at high 'nitriding potential' might be somewhat mitigated by a lower Ni content, and/or (partial) replacement of Ni with Mn.

3.3 Corrosion performance

OCP and potentiodynamic polarisation curves are plotted in **Fig. 8**. The stabilised OCP values are listed in **Table 3**. Corrosion potentials (E_{corr}) and current densities (I_{corr}) are derived from extrapolation of linear anodic/cathodic regions in the potentiodynamic polarisation curves and given in **Table 3**. In the potentiodynamic polarisation curves (**Fig. 8b-d**), E_{corr} shifts to higher potentials and I_{corr} shifts to lower current densities for the two Ni-stabilised ASSs (i.e. alloys AISI 304 and RA330) after TPN treatment at 400°C. The shifting of polarisation curves to the top-left regions of the plot correlates well to the "insertion" of nitrogen into matrix lattice interstitial sites, without segregation of host substitutional elements (such as Cr, Ni, or Mn). However, E_{corr} (and OCP) values do not vary significantly for the high-Mn AG17 after TPN at 400°C (**Fig. 8c**) – which might be related in part to the high pre-existing nitrogen level (ca. 0.5 wt.%; 2.0 at.%) already present in alloy AG17. The interstitial N-atoms released from aqueously-corroding surfaces (that form NH_4^+ ions [6, 8, 25, 42-46]) are likely to influence significantly the corrosion reaction system. While surface alloying of N-free ASSs (such as AISI 304 and RA330) with extremely high levels of interstitial N (i.e. to above 20 at.%) results in a more positive corrosion potential, a further increase in interstitial nitrogen in a high-N ASS substrate (in this case, untreated alloy AG17) does not appear to alter the corrosion potential significantly.

Additionally, E_{corr} increases both for AISI 304 (**Fig. 8b**) and for its Mn-rich alloy equivalents (such as AISI 202 [19, 20]) after low-temperature plasma nitriding – whereby surface layers all contain HCP-ε_N. It also worth mentioning that a thin top layer of 'ε-nitride' was revealed by Mössbauer spectroscopy on AISI 316L after nitriding, that appeared to increase E_{corr} during potentiodynamic polarisation [47]. However, a question remains as to whether or not the HCP-ε_N strips observed in this study would exhibit 'ε-nitride' characteristics under Mössbauer spectroscopy. Considering also the similar chemical composition between HCP-ε_N and FCC-γ_N (see **Fig. A1** and Ref. [18]), the presence (or not) of HCP-ε_N in the TPN-treated layer is most likely of no significant relevance to the 'unchanged E_{corr}' observed for AG17 after nitrogen supersaturation.

Table 3. OCP, E_{corr} and I_{corr} for three ASSs after TPN treatments (in 3.5 wt.% NaCl solution with a scanning rate of ~1.667 mV/s at ambient temperature)

Materials	**Treatments**	**OCP, V**	E_{corr}**, V**	I_{corr}**, ×10^{-6} A/cm^2**
AISI 304	Untreated	-0.09	-0.46	1.56
	TPN at 400°C	0.08	-0.26	0.17
	TPN at 450°C	-0.60	-0.72	1.42
AG17	Untreated	-0.36	-0.47	1.70
	TPN at 400°C	-0.33	-0.50	0.61
	TPN at 450°C	-0.66	-0.75	1.61
RA330	Untreated	-0.24	-0.41	1.05
	TPN at 400°C	-0.13	-0.33	0.88
	TPN at 450°C	-0.14	-0.33	1.13

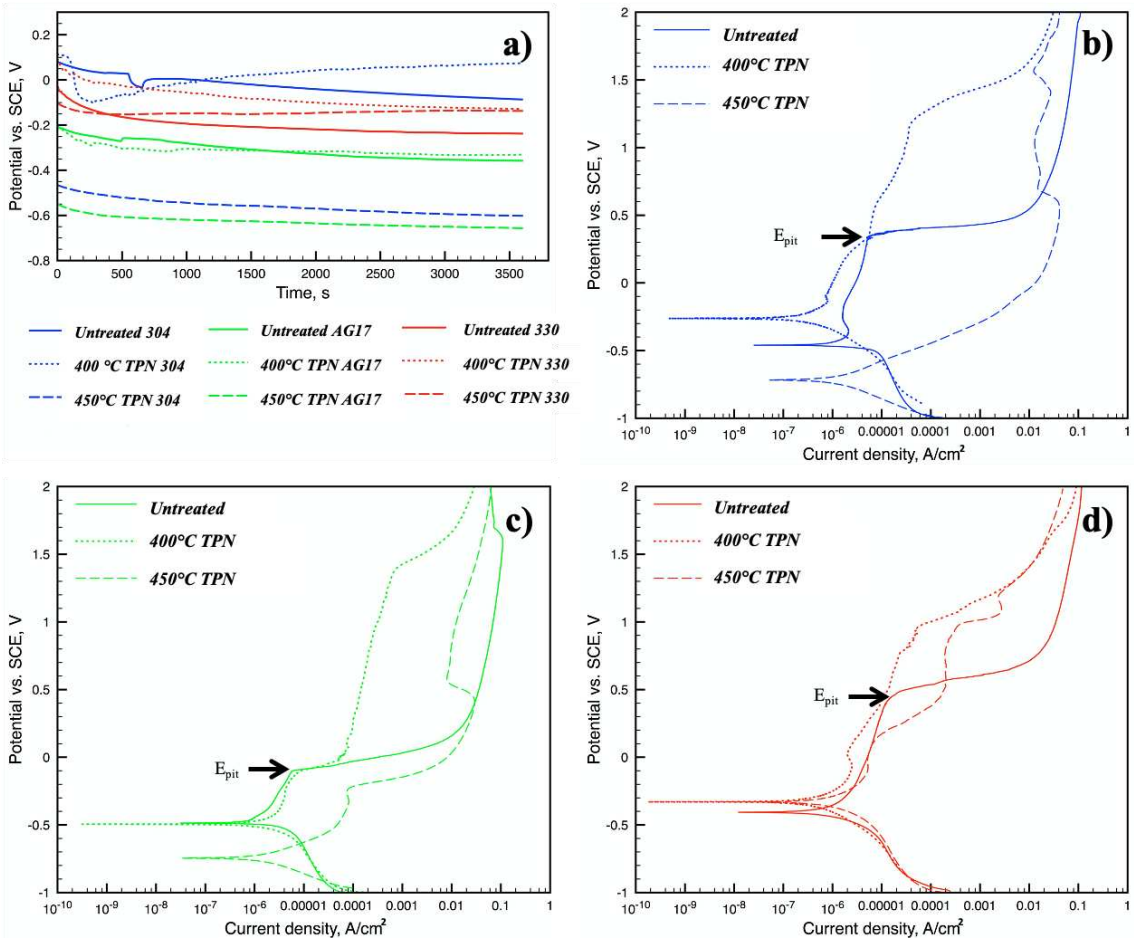

Fig. 8 a) OCP for all three ASSs before and after TPN treatment; and potentiodynamic polarisation curves for b) AISI 304, c) Staballoy® AG17 and d) RA330® before and after TPN treatments (in 3.5 wt.% NaCl solution with a scanning rate of ~1.667 mV/s at ambient temperature)

Stainless steels are known for their corrosion passivity, owing to the protective Cr_2O_3 surface film that forms in oxidising environments. The passivation of ASS in the anodic reaction region of the potentiodynamic polarisation curve requires more discussions (i.e. for dissolution of metallic elements into the electrolyte, $M \rightarrow M^{n+} + ne^-$ at the upper part of potentiodynamic curves above E_{corr}). A sharp increase in current density was observed for all three untreated ASSs above E_{pit} in **Fig. 8b-d**, due to breakdown of the passive oxide film and/or formation of corrosion pits (**Fig. 9a&b**). Following an order from Mn/N-stabilised to Ni-stabilised ASS, E_{pit} values are ~ -0.1V, ~ +0.3 V and ~ +0.5 V for alloys AG17, 304 and RA330, respectively. The high-Mn alloy AG17

542 showed the smallest passivation region and the high-Ni alloy RA330 presented the
543 largest passivation region. High Ni content in ASS appears beneficial therefore, in
544 sustaining a large passivation region and better resistance to pitting.
545
546 After TPN at 400°C, the passivation regions on all three ASSs were extended to higher
547 corrosion potentials, showing significantly reduced corrosion current densities in the
548 anodic reaction region. Although E_{pit} (at approximately -0.1V) appears similar on alloy
549 AG17 before and after 400°C TPN, the 400°C-treated AG17 experienced a 'secondary
550 passivation region', possessing current densities much lower than the untreated AG17
551 after the first 'breakdown' of passivation at ~ -0.1 V (**Fig. 8c**). No significant change
552 in surface morphology was seen for AG17 after corrosion testing. The "grainy
553 microstructure" morphology revealed in **Fig. 9c** was already seen before corrosion
554 testing, and can be attributed to a combined effect of plasma etching and "grain swelling"
555 [48] after TPN treatment. Preferential corrosion was not seen adjacent to the HCP-ε_N
556 strips. However, corrosion pits of ~20 μm diameter – although small in number – were
557 still found (as shown in **Fig. 9c**), that might be correlated to the isolated high-Cr regions
558 observed at grain boundaries (**Fig. A1**). In contrast to 400°C-treated AG17, localised
559 material surface degradation and loss was seen on γ_N-330 (showing black cavities under
560 OM in **Fig. 9d**), while the remaining surface of corroded γ_N-330 appears flat. SEM
561 imaging revealed localised corrosion at grain boundaries and slip/shear bands on
562 400°C-treated RA330 (inset in **Fig. 9d**), which could be associated with local Cr
563 segregation (see **Fig. A2** in **Appendix A**). Considering also the sharp edges between
564 the volume lost and the remaining surface (**Fig. 9d**), it is anticipated that some
565 metallurgical grains at surface spalled off after intergranular corrosion.
566

567 It worth mentioning the anodic polarisation was performed until a high voltage of +2V,
568 that ensures the polarisation curve passing beyond the wide passivation region (i.e. to
569 'break down' the passive films formed on stainless steels). A high corrosion current
570 density was 'forced' on 400°C-treated samples during the polarisation testing employed,
571 that contributes to the formation of corrosion pits and/or grain boundary corrosion.
572 Nevertheless, one may still argue that, upon surface nitrogen-supersaturation after low-
573 temperature nitriding treatment, pitting corrosion was inhibited and corrosion occurred
574 in a more general and uniform way for both alloys AG17 and RA330. This would
575 conventionally be attributed to the alkaline ammonium NH_4^+ ion – generated from
576 nascent nitrogen via the reaction $[N] + 4H^+ + 3e^- \rightarrow NH_4^+$ [46] – that neutralizes low
577 pH levels, retarding local acidification.

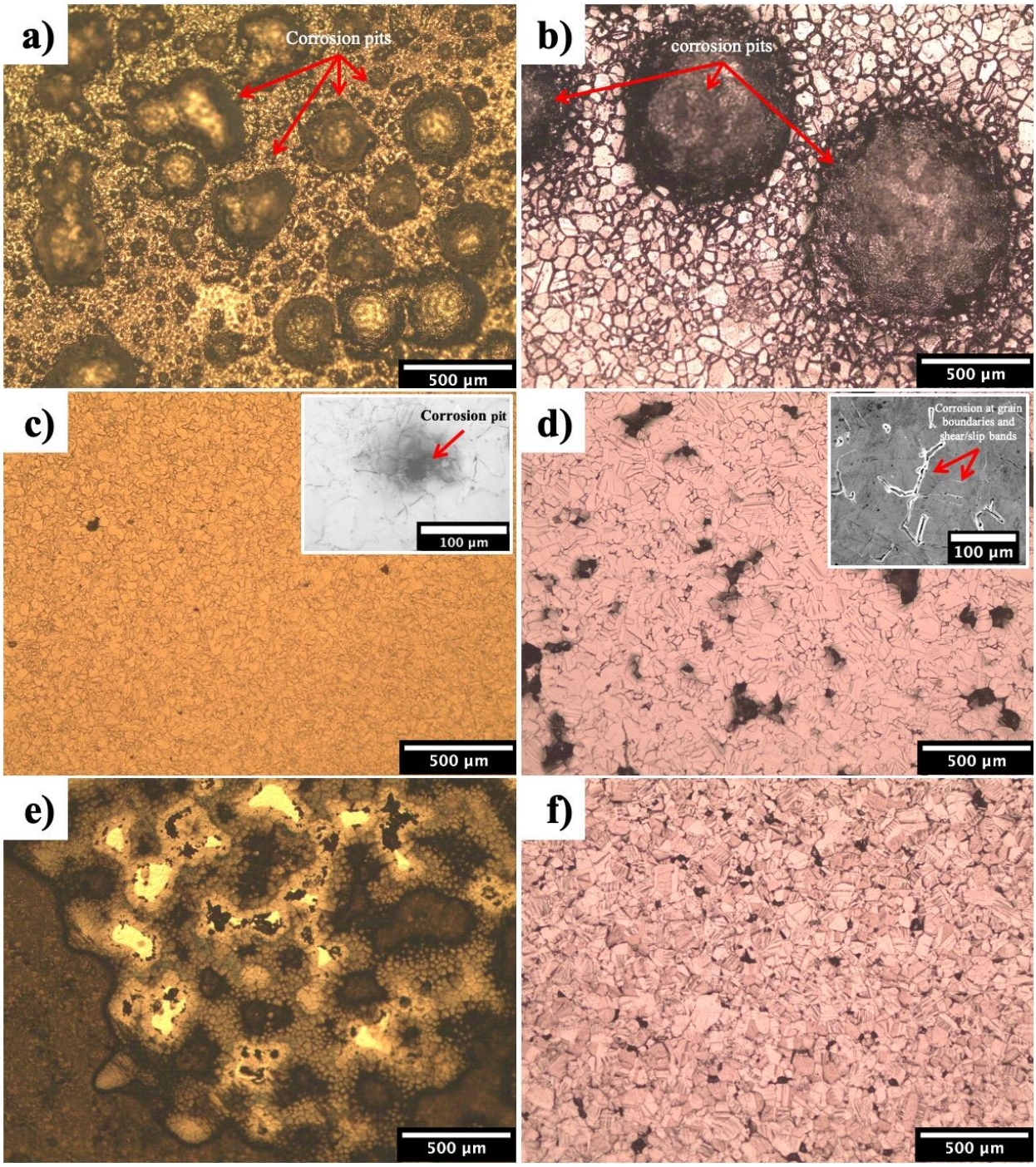

Fig. 9 OM images showing the morphologies of corrosion sites on a) untreated AG17, b) untreated RA330, c) 400°C TPN-treated AG17 (inset: OM image showing a corrosion pit), d) 400°C TPN-treated RA330 (inset: SEM image showing corrosion at grain boundaries), e) 450°C TPN-treated AG17, f) 450°C TPN-treated RA330.

For AISI 304 and AG17 after TPN at 450°C, polarisation curves are shifted to the bottom-right regions (less noble and with higher corrosion current densities) in **Fig. 8b**

586 **& c**. The degradation in corrosion performance is expected, given the decomposition
587 of γ_N to cellular mixture of [CrN + α] on alloys 304 and AG17 after TPN at 450°C. In
588 contrast, under equivalent TPN treatment at 450°C, alloy RA330 showed an increase
589 in E_{corr} and an extended passivation region (**Fig. 8d**), which could be attributed to the
590 sluggish decomposition mechanism of the high-Ni γ_N on this substrate material [17].
591 Most importantly, while the corroded surface on 450°C TPN-treated AG17 is covered
592 with corrosion products (**Fig. 9e**), the corrosion surface on 450°C TPN-treated RA330
593 appears "clean" and shows similar morphology to 400°C TPN-treated RA330 with
594 uniform corrosion being the corrosion mechanism for γ_N-330 grains and local corrosion
595 at planar defects (c.f. **Fig. 9d&f**). No round corrosion pits were seen. In other words,
596 compared to Cr-nitride formation and decomposition of γ_N on alloy 304 or AG17 at
597 ~450°C, the ability to form a continuous protective Cr-oxide film was unharmed for
598 γ_N-330 grains after TPN at 450°C, due apparently to no significant Cr redistribution in
599 γ_N (**Fig. 4**). The local, short-range redistribution of Si does not impose a significant
600 degradation in material corrosion performance. However, we anticipate that Cr-nitrides
601 would eventually form in γ_N-330 – either after prolonged treatment time or at higher
602 treatment temperature – and that this would deteriorate material corrosion performance,
603 in a similar way to the other two alloys investigated.
604

605 **Conclusions**

606 In this study, the tribological behaviour and corrosion performance of three austenitic
607 stainless steels, AISI 304 (Fe-18Cr-8Ni-2Mn), Staballoy® AG17 (Fe-17Cr-20Mn-
608 0.5N, in wt.%) and RA330® (Fe-19Cr-35Ni-1.2Si, in wt.%), were evaluated and

609 compared after triode plasma nitriding at 400°C and 450°C for 20hrs. The results can
610 be summarised as follows:

611 - TPN treatment at 400°C significantly hardened the alloy surfaces via nitrogen-
612 interstitial supersaturation, providing a two to three orders of magnitude reductions
613 in wear rate for all three ASSs under the selected dry sliding wear test conditions.
614 - Surface maximum nitrogen concentration, micro-indentation hardness
615 enhancement and reciprocating-sliding wear rate reduction after TPN of ASSs at
616 400°C appear to follow an improving trend from high-Ni to high-Mn substrate
617 alloy content, at a nominal alloy Cr-content of ~18 wt.%.
618 - Under SEM investigation, extensive 'lines' (strips) could be seen in γ_N-AG17 after
619 TPN at 400°C, which were identified by further TEM studies as being HCP-ε_N.
620 The presence of HCP-ε_N in γ_N-AG17 appears to correlate to an enhancement in
621 surface hardness and improved wear resistance after TPN at 400°C. This might be
622 owing to a higher nitrogen absorption (for high-Mn ASS) and to complex strain
623 hardening mechanisms (that involve TRIP effects).
624 - The micro-cracks seen after sliding wear on the high-Ni γ_N-330 layer suggest high
625 residual stress and poor layer toughness. However, such brittleness features are
626 absent on alloy AG17 after TPN treatment under equivalent conditions, which
627 could be associated to the difference in ASS substrate composition (i.e. lower Ni
628 content) and the different plasticity mechanisms involved.
629 - Surface nitrogen supersaturation at 400°C extends the corrosion passivation region,
630 and delays (and improves resistance to) pitting corrosion during potentiodynamic
631 polarisation in 3.5 wt.% NaCl aqueous solution.

- Corresponding to their homogenous elemental distribution (compared to the surrounding γ_N matrix), no detrimental influence on corrosion performance could be seen for the HCP-ε_N regions found in the γ_N-AG17 layer formed at 400°C.
- In good agreement to γ_N destabilization and Cr-nitride precipitation, a degradation in corrosion performance was evident for AISI 304 and alloy AG17 after TPN at 450°C.
- In contrast, a Si-rich Cr-containing precipitate was revealed in alloy RA330 at the higher nitriding temperature of 450°C. Apart from highly-localised Cr-segregation (and consequent local corrosion) at isolated slip/shear bands and grain boundaries, corrosion pits were not seen and a rather uniform corrosion was observed within γ_N-330 grains at 450°C. In addition to a high Ni content at ~35 wt.%, Si alloying addition at levels more than the 'typical' ~0.3 wt.% found in many ASSs (1.2 wt.% in the case of the high-temperature oxidation- and carburization-resistant RA330) appears beneficial in extending the improved corrosion performance of γ_N to higher TPN treatment temperatures (thus permitting shorter treatment times, for equivalent nitriding efficacy).

Acknowledgements

This research did not receive any specific grant from funding agencies in the public, commercial, or not-for-profit sectors. We would however like to thank ATI Allvac (Sheffield) Ltd. for their kind provision of Staballoy AG17® and NeoNickel (Blackburn) Ltd. for the supply of RA 330® for this study.

Appendix A

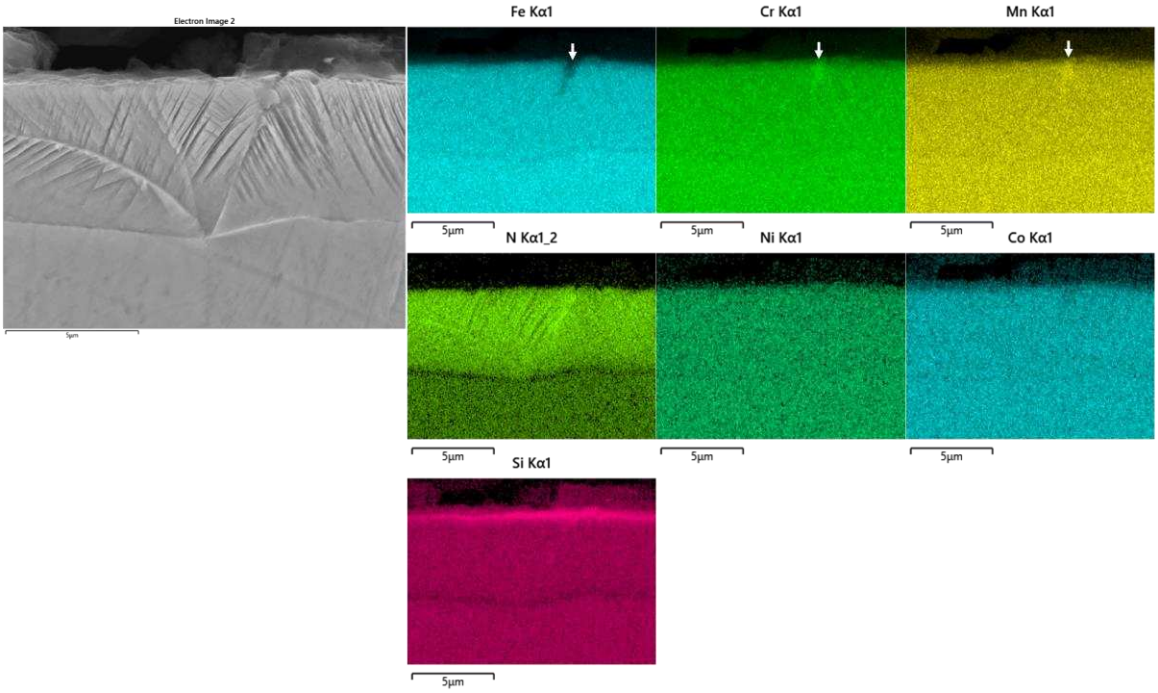

Fig. A1 SEM-EDX mapping for AG17 after TPN treatment at 400°C for 20hrs; a low-Fe, high-Cr region is indicated by arrow.

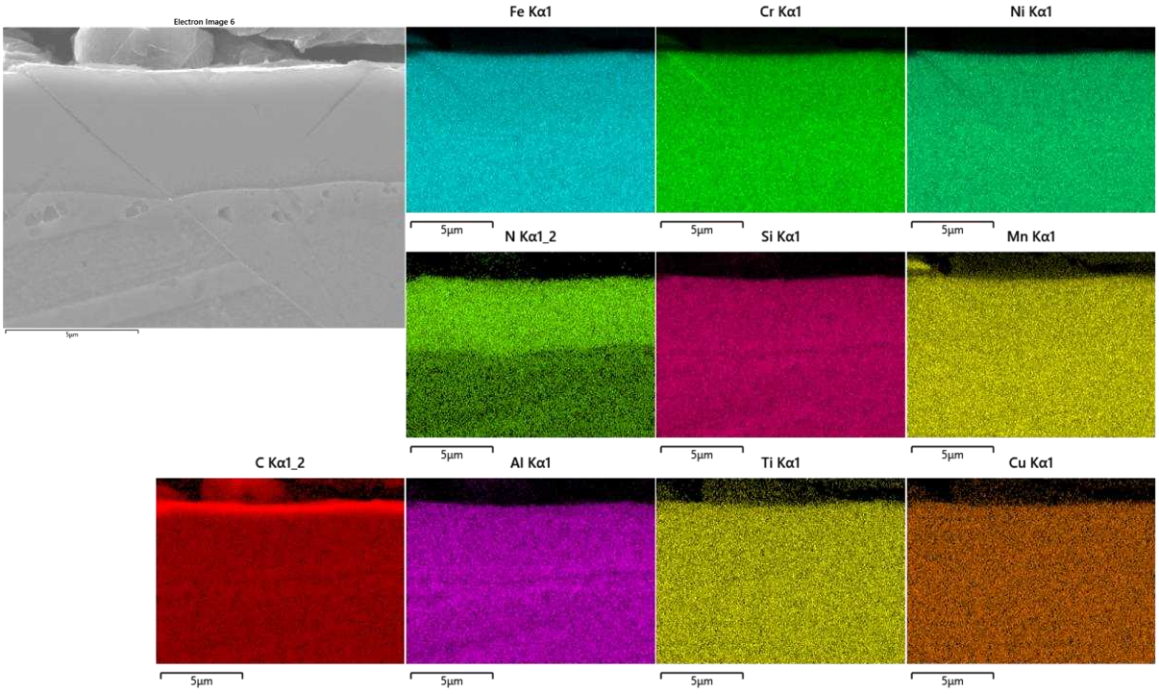

Fig. A2 SEM-EDX mapping for RA330 after TPN treatment at 400°C for 20hrs; Cr segregation is seen at grain boundary

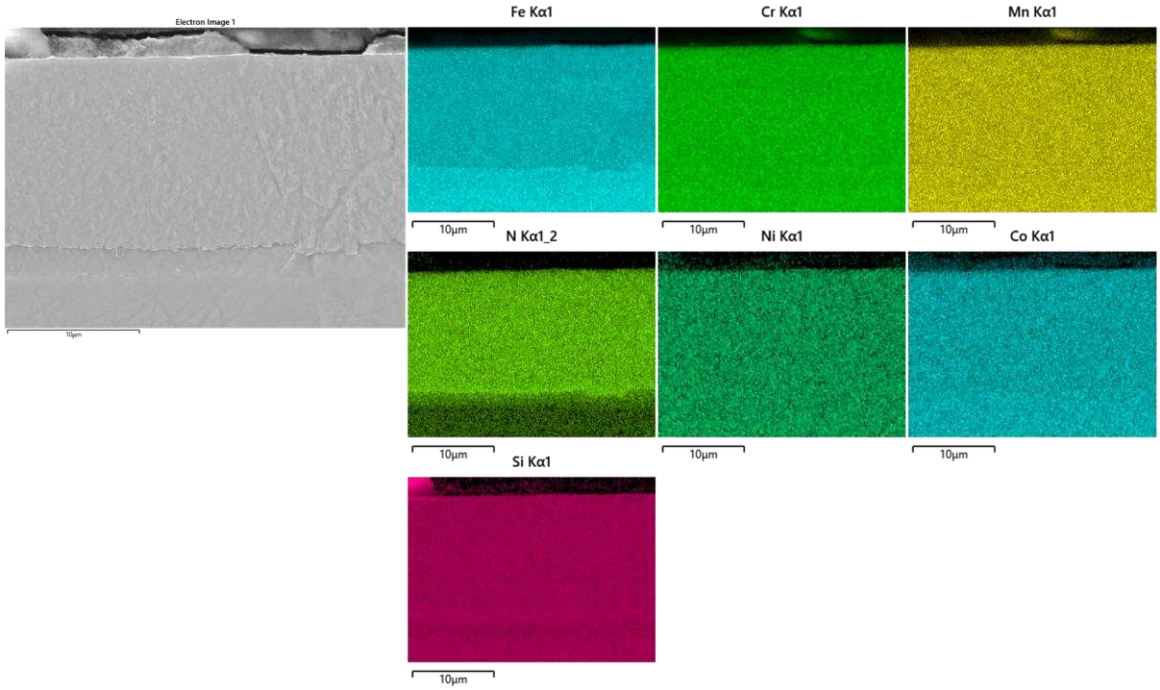

662

663 **Fig. A3** SEM-EDX mapping for AG17 after TPN treatment at 450°C for 20hrs

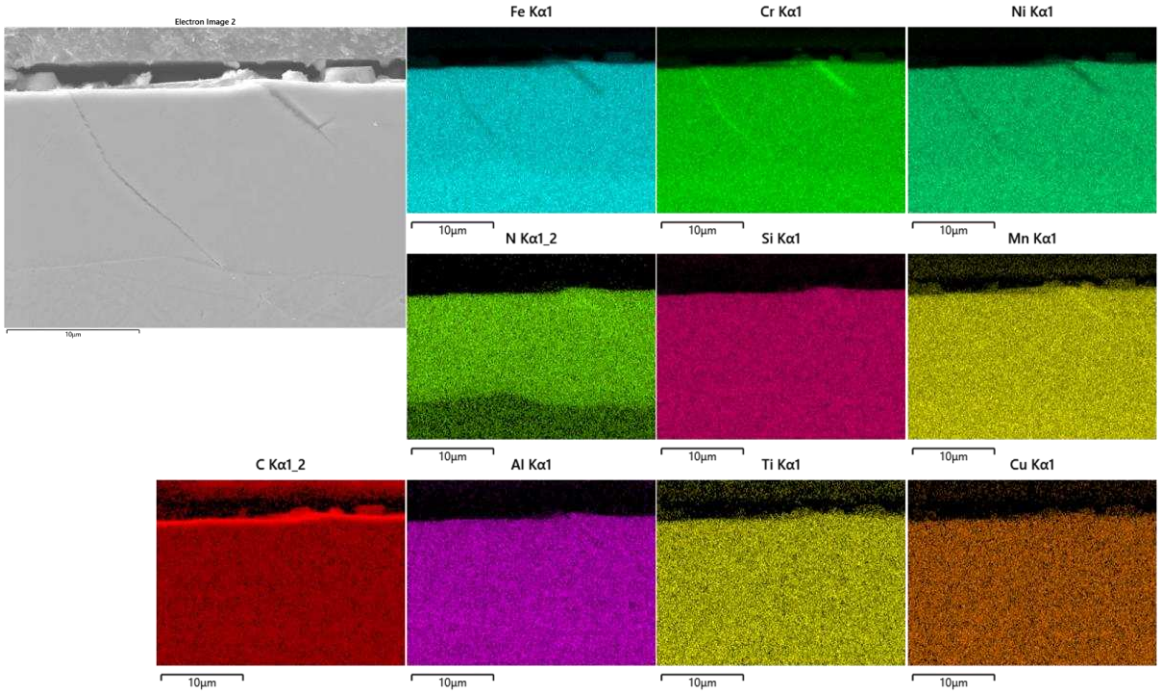

664

665 **Fig. A4** SEM-EDX mapping for RA330 after TPN treatment at 450°C for 20hrs; Cr-

666 segregation is observed at grain boundary and shear/slip band

667

668

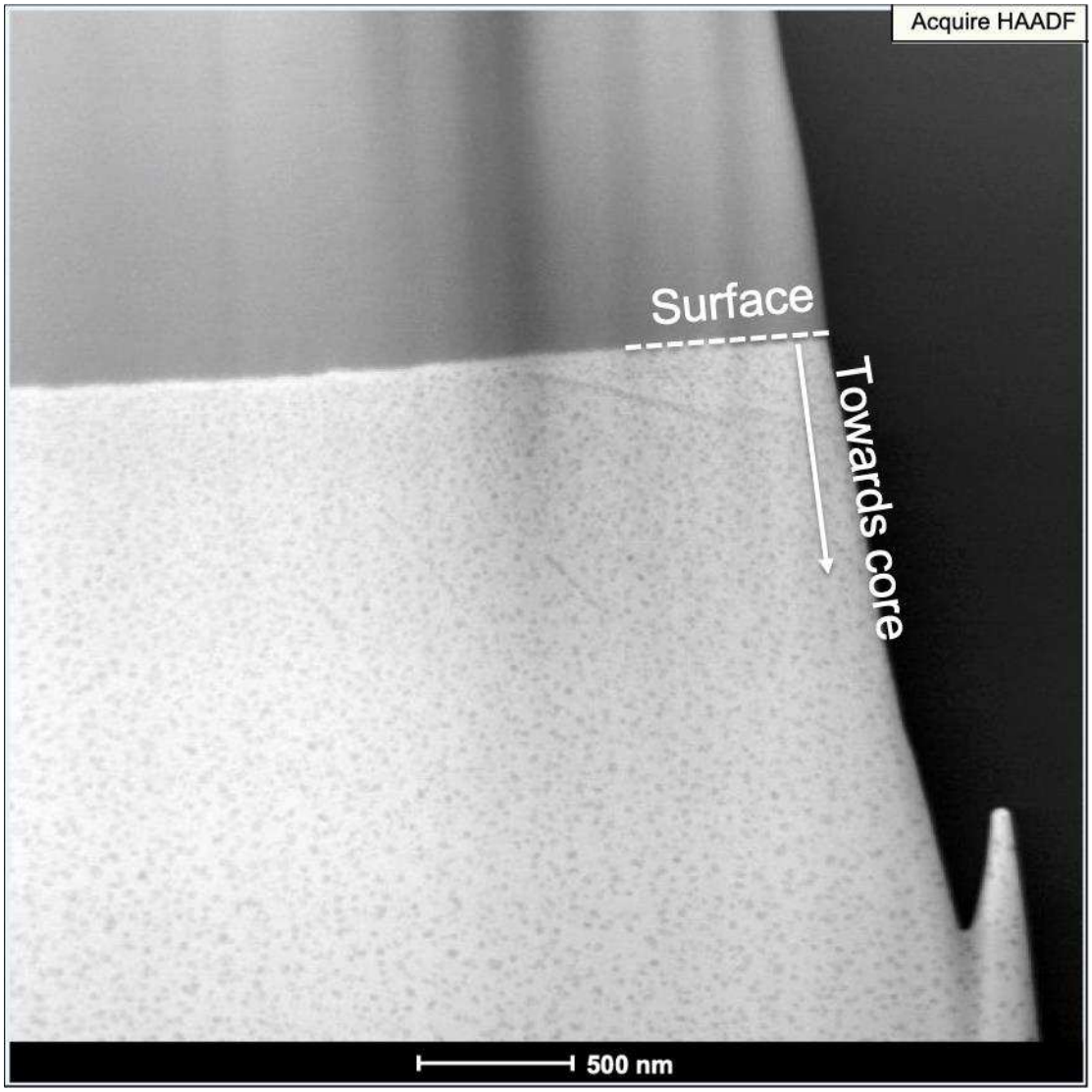

Fig. A5 STEM image for RA330 after TPN treatment at 450°C for 20hrs, showing the distribution of S-rich nanoprecipitates over a rather large area

680 **Appendix B**

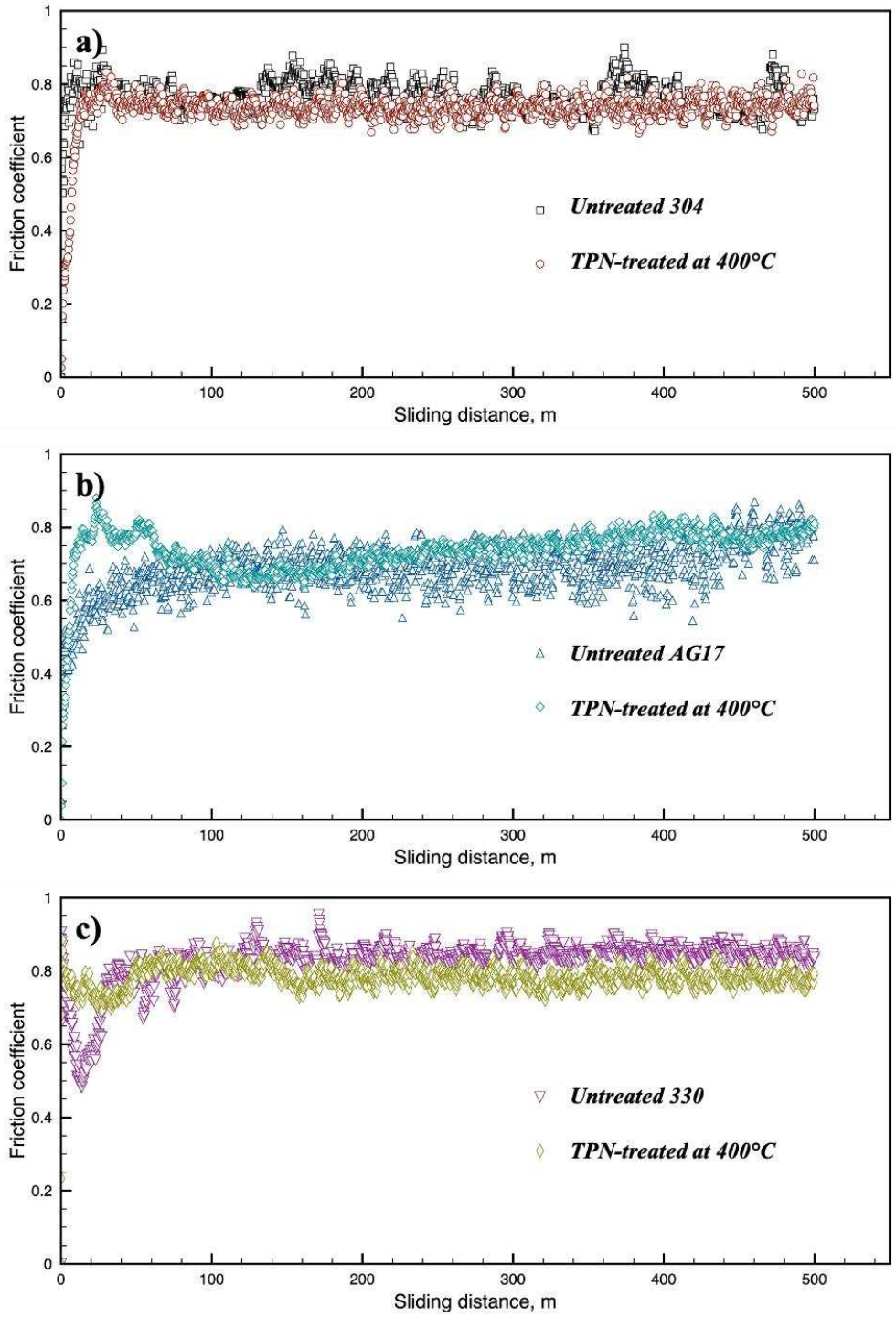

681

682 **Fig. B1** Friction coefficient evolution with sliding wear distance for the three

683 investigated stainless steel alloys, before and after TPN treatment at 400°C

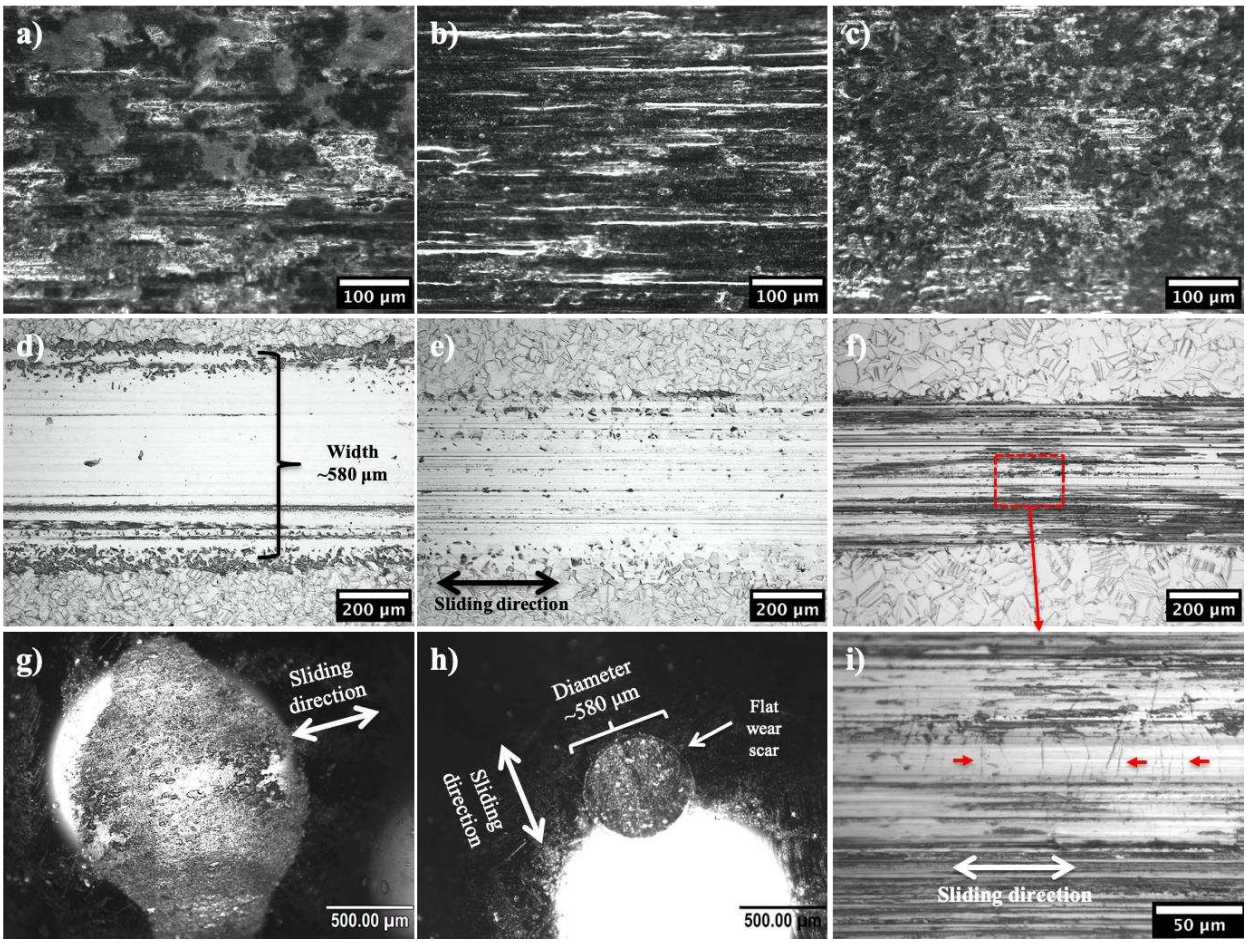

Fig. B2 OM images showing the morphology of the sliding wear track on a) untreated AISI 304, b) untreated Staballoy AG17, c) untreated RA330, d) 400°C TPN-treated AISI 304, e) 400°C TPN-treated Staballoy AG17, f) 400°C TPN-treated RA330 (sliding direction is horizontal in **Fig. B2a-f**); OM images showing the wear site on the WC-Co balls which slided against g) untreated AISI 304, h) 400°C TPN-treated AISI 304; i) OM image showing the micro-cracks that lies perpendicular to sliding direction in the wear track on 400°C TPN-treated RA330.

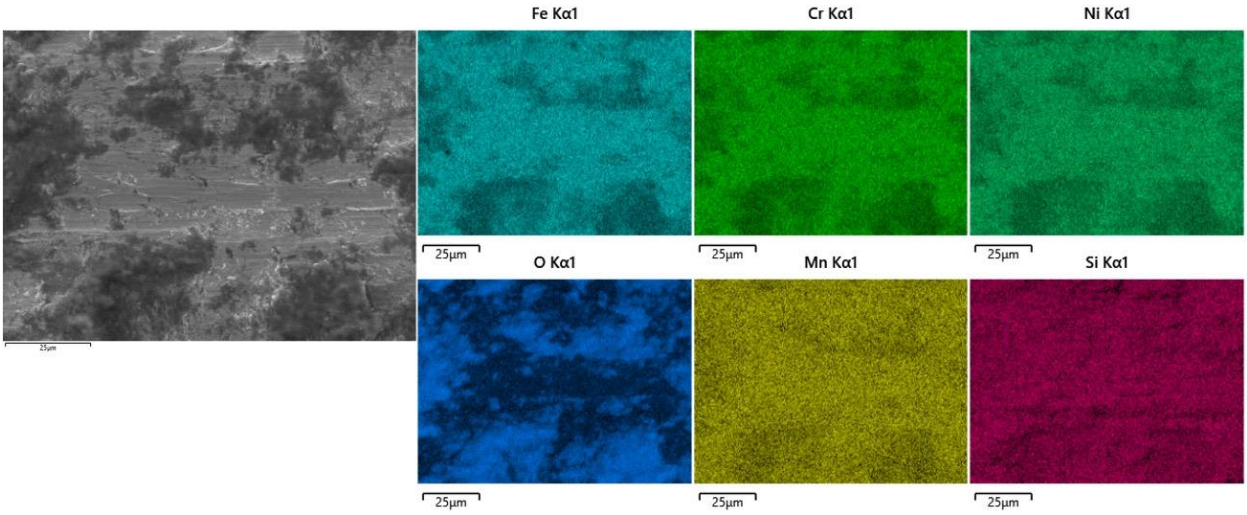

695

696 **Fig. B3** SEM-EDX mapping for the sliding wear track on untreated RA330

697

698

References

[1] K.L. Hsu, T.M. Ahn, D.A. Rigney, Friction, wear and microstructure of unlubricated austenitic stainless steels, Wear, 60 (1980) 13-37.
[2] A.F. Smith, The friction and sliding wear of unlubricated 316 stainless steel at room temperature in air, Wear, 96 (1984) 301-318.
[3] Z.L. Zhang, T. Bell, Structure and corrosion resistance of plasma nitrided stainless steel, Surf. Eng., 1 (1985) 131-136.
[4] Y. Sun, T. Bell, Sliding wear characteristics of low temperature plasma nitrided 316 austenitic stainless steel, Wear, 218 (1998) 31-42.
[5] C.X. Li, T. Bell, Sliding wear properties of active screen plasma nitrided 316 austenitic stainless steel, Wear, 256 (2004) 1144-1152.
[6] C.X. Li, T. Bell, Corrosion properties of active screen plasma nitrided 316 austenitic stainless steel, Corros. Sci., 46 (2004) 1527-1547.
[7] L. Poirier, Y. Corre, J.P. Lebrun, Solutions to improve surface hardness of stainless steels without loss of corrosion resistance, Surf. Eng., 18 (2002) 439-442.
[8] J. Buhagiar, H. Dong, Corrosion properties of S-phase layers formed on medical grade austenitic stainless steel, J. Mater. Sci. Mater. Med., 23 (2012) 271-281.
[9] T. Christiansen, M.A.J. Somers, Controlled dissolution of colossal quantities of nitrogen in stainless steel, Metall. Mater. Trans. A, 37A (2006) 675-682.
[10] H. Dong, S-phase surface engineering of Fe-Cr, Co-Cr and Ni-Cr alloys, Int. Mater. Rev., 55 (2010) 65-98.
[11] Y. Cao, F. Ernst, G.M. Michal, Colossal carbon supersaturation in austenitic stainless steels carburized at low temperature, Acta Mater., 51 (2003) 4171-4181.
[12] S. Collins, P. Williams, in: Advanced Materials and Process, ASM International, 2006, pp. 32-33.
[13] K. Ichii, K. Fujimura, T. Takase, Structure of the ion-nitrided layer of 18-8 stainless steel, Technology Reports of Kensai University, 27 (1986) 135-144.
[14] S.P. Hannula, O. Nenonen, J.-P. Hirvonen, Surface structure and properties of ion-nitrided austenic stainless steels, Thin Solid Films, 181 (1989) 343-350.
[15] A. Leyland, D.B. Lewis, P.R. Stevenson, A. Matthews, Low temperature plasma diffusion treatment of stainless steels for improved wear resistance, Surf. Coat. Technol., 62 (1993) 608-617.
[16] T. Christiansen, M.A.J. Somers, On the crystallographic structure of S-phase, Scripta Mater., 50 (2004) 35-37.
[17] X. Tao, X. Liu, A. Matthews, A. Leyland, The influence of stacking fault energy on plasticity mechanisms in triode-plasma nitrided austenitic stainless steels: Implications for the structure and stability of nitrogen-expanded austenite, Acta Mater., 164 (2019) 60-75.
[18] X. Tao, J. Qi, M. Rainforth, A. Matthews, A. Leyland, On the interstitial induced lattice inhomogeneities in nitrogen-expanded austenite, Scripta Mater., 185 (2020) 146-151.
[19] F. Borgioli, E. Galvanetto, T. Bacci, Low temperature nitriding of AISI 300 and 200 series austenitic stainless steels, Vacuum, 127 (2016) 51-60.
[20] F. Borgioli, A. Fossati, G. Matassini, E. Galvanetto, T. Bacci, Low temperature glow-discharge nitriding of a low nickel austenitic stainless steel, Surf. Coat. Technol., 204 (2010) 3410-3417.
[21] J. Buhagiar, X. Li, H. Dong, Formation and microstructural characterisation of S-phase layers in Ni-free austenitic stainless steels by low-temperature plasma surface alloying, Surf. Coat. Technol., 204 (2009) 330-335.

[22] G. Maistro, S.A. Pérez-García, M. Norell, L. Nyborg, Y. Cao, Thermal decomposition of N-expanded austenite in 304L and 904L steels, Surf. Eng., 33 (2017) 319-326.
[23] A. Leyland, K.S. Fancey, A.S. James, A. Matthews, Enhanced plasma nitriding at low pressures: a comparative study of d.c. and r.f. techniques, Surf. Coat. Technol., 41 (1990) 295-304.
[24] A. Leyland, K.S. Fancey, A. Matthews, Plasma nitriding in a low pressure triode discharge to provide improvements in adhesion and load support for wear resistant coatings, Surf. Eng., 7 (1991) 207-215.
[25] A. Fossati, F. Borgioli, E. Galvanetto, T. Bacci, Corrosion resistance properties of glow-discharge nitrided AISI 316L austenitic stainless steel in NaCl solutions, Corros. Sci., 48 (2006) 1513-1527.
[26] X. Xu, Z. Yu, L. Wang, J. Qiang, Z. Hei, Phase depth distribution characteristics of the plasma nitrided layer on AISI 304 stainless steel, Surf. Coat. Technol., 162 (2003) 242-247.
[27] C. Templier, J.C. Stinville, P. Villechaise, P.O. Renault, G. Abrasonis, J.P. Riviere, A. Martinavicius, M. Drouet, On lattice plane rotation and crystallographic structure of the expanded austenite in plasma nitrided AISI 316L steel Surf. Coat. Technol., 204 (2010) 2551-2558.
[28] J.C. Stinville, C. Tromas, P. Villechaise, C. Templier, Anisotropy changes in hardness and indentation modulus induced by plasma nitriding of 316L polycrystalline stainless steel, Scripta Mater., 64 (2011) 37-40.
[29] B.K. Brink, K. Stahl, T.L. Christiansen, J. Oddershede, G. Winthiner, M.A.J. Somers, On the elusive crystal structure of expanded austenite, Scripta Mater., 131 (2017) 59-62.
[30] K.M. Eliasen, T.L. Christiansen, M.A.J. Somers, Low temperature gaseous nitriding of Ni based superalloys, Surf. Eng., 26 (2010) 248-255.
[31] A.L. Schaeffler, Consitution diagram for stainless steel weld metal, Metal Progress, 56 (1949) 680-680B.
[32] T. Christiansen, K.L. Dahm, M.A.J. Somers, New stainless steel alloys for low temperature surface hardening, BHM Berg- und Hüttenmännische Monatshefte, 160 (2015) 406-412.
[33] A. Phongphiphat, C. Ryu, Y.B. Yang, K.N. Finney, A. Leyland, V.N. Sharifi, J. Swithenbank, Investigation into high-temperature corrosion in a large-scale municipal waste-to-energy plant, Corros. Sci., 52 (2010) 3861-3874.
[34] W.-T. Tsai, Y.-N. Wen, J.-T. Lee, H.-Y. Liou, W.-F. Wang, Effect of silicon addition on the microstructure and corrosion behavior of sintered stainless steel, Surf. Coat. Technol., 34 (1988) 209-217.
[35] T. Bell, C.X. Li, Plasma thermochemical processing of austenitic stainless steel for combined wear and corrosion resistance, SAE Technical Paper (2002) 2002-2001-1337.
[36] D. Hoeft, B.A. Latella, K.T. Short, Residual stress and cracking in expanded austenite layers, J. Phys.: Condens. Matter, 17 (2005) 2547-3558.
[37] T. Bell, Y. Sun, Low-temperature plasma nitriding and carburising of austenitic stainless steels, Heat Treat. Met., 29 (2002) 57-64.
[38] T.L. Christiansen, M.A.J. Somers, Low-temperature gaseous surface hardening of stainless steel: the current status, Int. J. Mater. Res., 100 (2009) 1361-1377.
[39] T. Christiansen, T.S. Hummelshoj, M.A.J. Somers, Expanded austenite, crystallography and residual stress, Surf. Eng., 26 (2010) 242-247.
[40] T. Christiansen, M.A.J. Somers, Low temperature gaseous nitriding and carburising of stainless steel, Surf. Eng., 21 (2005) 445-455.
[41] X. Tao, Investigations on the role of Cr, Mn and Ni on the formation, structure, and metastability of nitrogen-expanded austenite on Fe-based austenitic alloys under triode-plasma

nitriding, PhD Thesis, Department of Materials Science and Engineering, University of Sheffield (2018).
[42] X.M. Zhu, M.K. Lei, Pitting corrosion resistance of high nitrogen f.c.c. phase in plasma source ion nitrided austenitic stainless steel, Surf. Coat. Technol., 131 (2000) 400-403.
[43] M.K. Lei, X.M. Zhu, In vitro corrosion resistance of plasma source ion nitrided austenitic stainless steels, Biomaterials, 22 (2001) 641-647.
[44] X.Y. Li, H. Dong, Effect of annealing on corrosion behaviour of nitrogen S phase in austenitic stainless steel, Mater. Sci. Technol., 19 (2003) 1427-1434.
[45] L.C. Gontijo, R. Machado, S.E. Kuri, L.C. Casteletti, P.A.P. Nascente, Corrosion resistance of the layers formed on the surface of plasma-nitrided AISI 304L steel, Thin Solid Films, 515 (2006) 1093-1096.
[46] R.F.A. Jargelius-Pettersson, Electrochemical investigation of the influence of nitrogen alloying on pitting corrosion of austenitic stainless steels, Corros. Sci., 41 (1999) 1639-1664.
[47] M. Olzon-Dionysio, D. Olzon-Dionysio, M. Campos, W.T. Shigeyosi, S.D. de Souza, S. de Souza, Corrosion resistance of AISI 316L plasma nitrided at different temperatures and times, Hyperfine Interact., 240 (2019) 26.
[48] J.C. Stinville, C. Templier, P. Villechaise, L. Pichon, Swelling of 316L austenitic stainless steel induced by plasma nitriding, J. Mater. Sci., 46 (2011) 5503-5511.